

Development and application of the Ascent-Drift-Descent Radiosonde System (ADDRS)

Xiaozhong Cao*¹, Qiyun Guo^{2,3,4}, Haowen Luo^{2,3,4}, Rongkang Yang^{2,3,4}, Guo Jianping⁵, Jincheng Wang⁶, Die Xiao⁷, Yinfeng Liu⁸, Zhongliang Sun⁹, Shijun Liu¹⁰, Sijie Chen¹¹, Anfan Huang^{2,3,4}, Peng Zhang*^{2,3,4}

¹ China Meteorological Administration, Beijing, China;

² Meteorological Observation Centre of China Meteorological Administration, Beijing, China;

³ State Key Laboratory of Environment Characteristics and Effects for Near-space, Beijing, China;

⁴ Engineering Technology Research Center for Meteorological Observation of CMA, Beijing, China;

⁵ Chinese Academy of Meteorological Sciences, Beijing, China;

⁶ CMA Earth System Modeling and Prediction Centre (CEMC), Beijing, China;

⁷ Hunan Key Laboratory of Near-space Meteo-ballon Materials and Technology, Zhuzhou Research & Design Institute Co, Ltd, Zhuzhou, China;

⁸ Beijing Huayun Orient Detection Technology Co, Ltd., Beijing, China;

⁹ Allystar Technology (Shenzhen) Co.LTD. , Shenzhen, China;

¹⁰ Department of Advanced Technology Training of China Meteorological Administration, Beijing, China;

¹¹ National Satellite Meteorological Centre of China Meteorological Administration, Beijing, China;

Corresponding author: Xiaozhong Cao, caoxzh@cma.gov.cn, Peng zhang, zhangp@cma.gov.cn.

ABSTRACT. Balloon-borne radiosonde observations constitute a crucial component of meteorological sounding, which conducts a ground to upper-air “ascent phase” sounding. This paper introduces the Ascent-Drift-Descent Radiosonde System (ADDRS), an innovative system characterized by three observation phases—'Ascent-Drift-Descent' (ADD)—in which all three phases of sounding observation are executed through single balloon launch. Several key technologies were successfully developed, including the carrier (dual-mode balloon), the payload (System-on-Chip (SoC) module for radiosonde), Ground to upper-air data reception and control command transmission and data processing framework based on 'Internet cloud + Instrument terminal' was established. Data quality control methods and data assimilation techniques of ADDRS were also developed. An interactive experiment encompassing observations and forecasting was conducted to evaluate the quality of experimental data at each phase of ADDRS. Numerical assimilation and forecasting experiments showed a positive (albeit not yet statistically significant) impact on forecast quality for both general cases and for Tropical cyclone cases. The pre-operational launching and assimilation of more than 100 such radiosondes started on 1 July 2024 and provided data over one year, and the number of stations continues to grow.

1. Introduction

The upper-air meteorological sounding system (hereinafter referred to as 'sounding') constitutes a key element within comprehensive meteorological measurement framework (Ingleby et al., 2016). It is responsible for gathering data on various meteorological elements such as temperature, humidity, pressure, wind speed, and wind direction from the surface up to heights of 30 km and beyond upper atmosphere (DuBois et al., 2002). This

37 system provides vertically observed meteorological data for weather forecasting, numerical weather prediction,
38 climate projection, scientific research, and the inspection and calibration of ground-based remote sensing
39 equipment (Seidel et al., 2009; Fujiwara et al., 2025). The integration of radiosonde technology with balloon-
40 borne soundings emerged in the 1930s, with early operational systems deployed in the 1940s; this technology
41 has since served as a primary tool for direct measurements of upper-air meteorological elements below 30 km
42 and is widely utilized on a global scale (Pettifer 2009; Gallice et al., 2011).

43 For nearly a century, these radiosondes have utilized the direct measurement method of “one balloon
44 launched, one profile”. The radiosonde ascends at a certain speed with the balloon expanding in volume due to
45 decreasing air pressure as altitude increases. Upon reaching a specific altitude, the balloon bursts, concluding
46 the measurement process. This methodology confines effective observations to the radiosonde's ascent phase
47 (Haig et al., 1958). The disposable nature of radiosondes and balloons necessitates significant costs for multiple
48 deployments. Consequently, economic constraints have led to reductions in sounding operations, such as
49 Russia's temporary reduction of launches from twice to once daily in 2015, impacting the forecasting accuracy
50 of numerical prediction models across Northern Hemisphere countries (Ingleby et al., 2016).

51 In recent decades, satellite soundings have played an increasing role in Numerical Weather Prediction
52 (NWP) and are now the observations contributing most to forecast skill (Bauer et al., 2015; Bormann et al.,
53 2019; WMO, 2024). While radio occultation data has gained importance as a reference standard (Bauer et al.,
54 2014), radiosonde profiles still provide a crucial contribution to forecast skill and are fundamental for the
55 calibration and validation of satellite soundings (Newman et al., 2020). But the temporal resolution of global
56 radiosonde observations data remains limited, posing a significant challenge to its capacity in fulfilling the
57 requirements of routine forecasting. A notable concern arises from the scarcity of direct measurement data
58 during periods characterized by frequent severe convective activity, particularly in the hours immediately
59 following noon. Several studies have demonstrated that the frequent acquisition of descent radiosonde data can
60 enhance the accuracy of numerical weather forecasting. Dropsonde data assimilation has been shown to
61 hurricane trajectory forecast errors associated with an approximate reduction of 10-15% in specific contexts,
62 such as short-term (0-48h) predictions over ocean basins using the GFS model, as demonstrated in multi-year
63 statistical analyses (Ingleby, 2021; Cohn et al., 2013; Wang et al., 2015).

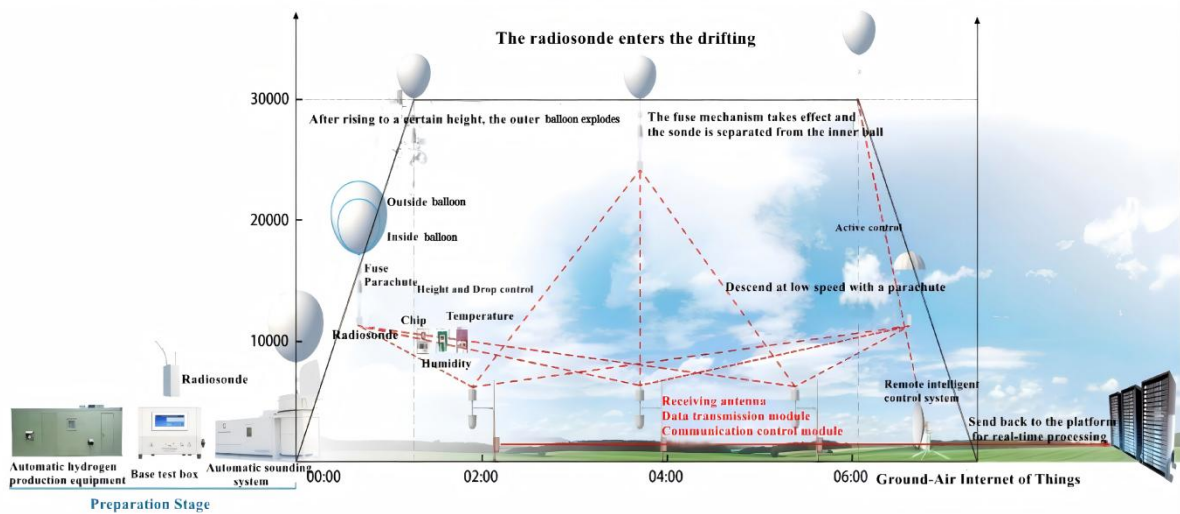
64 Additionally, several institutions are actively investigating techniques to obtain multiple radiosonde data
65 points from a solitary balloon launch. Illustrative projects include the multidisciplinary analysis of the African
66 monsoon and the measurement system research and forecasting experiments conducted in the Asia-Pacific
67 region, which utilize balloons to conduct drop soundings as they drift with stable upper-air winds over the
68 ocean (Raman et al., 2011; Johnson et al., 2024). Similarly, the Centre National d'Etudes Spatiales (CNES) of the
69 French Space Agency, has developed a Super Pressure Balloon (SPB) capable of floating in the stratosphere for
70 over three months (Roth et al., 2022). Additionally, the Tata Institute of Fundamental Research Balloon Facility
71 (TIFR-BF) in India has also contributed to this field by developing comparable systems (Anand et al., 2021;
72 Vernier et al., 2018; Vernier., 2022). While early stratospheric balloon systems faced questions about their long-
73 term feasibility for operational data collection due to cost and ascent rate limitations (WMO-No. 8., 2025). For
74 temperature and humidity, slower ascent can reduce the accuracy of vertical resolution due to issues like sensor
75 response time and radiative errors. However, for wind vectors, especially crucial upper-level winds, GPS-based

76 positioning provides high-precision data less affected by the ascent rate. The development of a new generation
 77 of commercial balloon systems has been changing this landscape.

78 Another conducted an extensive analysis by compiling four years of radiosonde data collected without
 79 parachutes across various seasons and altitudes, highlighting the scientific value of descent data (Ratnam et al.,
 80 2014; Ingleby et al., 2022). On account of the sounding process of ascending and descending at the same station
 81 has restricted its potential in conducting adaptive or targeting observation on typhoon forecast (Tan et al., 2006).
 82 This paper introduces a new sounding technology—the Ascent-Drift-Descent Radiosonde System (ADDRS).
 83 This system can improve the spatial and temporal frequency of soundings and provides an additional vertical
 84 profile as well as maintaining cost-effective, which acquires radiosonde measurement data throughout three
 85 phases—'Ascent-Drift-Descent' (ADD)—all with a single balloon launch (Cao et al., 2019).

86 **2. Synopsis of the Ascent-Drift-Descent Radiosonde System (ADDRS)**

87 The ADDRS was developed by the Meteorological Observation Centre of the China Meteorological
 88 Administration (MOC of CMA) with other relevant organizations in China (hereinafter referred to as the
 89 'ADDRS research team'). It undertakes a three-phase upper-air measurement (Fig. 1). In addition to the ascent
 90 phase of the current sounding system, ADDRS enables sounding during both the drift and descent phases. This
 91 innovative approach completes three phases of sounding with only a single balloon launch, representing a
 92 significant advancement in comparison with the traditional upper-air sounding method that has been utilized for
 93 nearly a century (Cao et al., 2022).

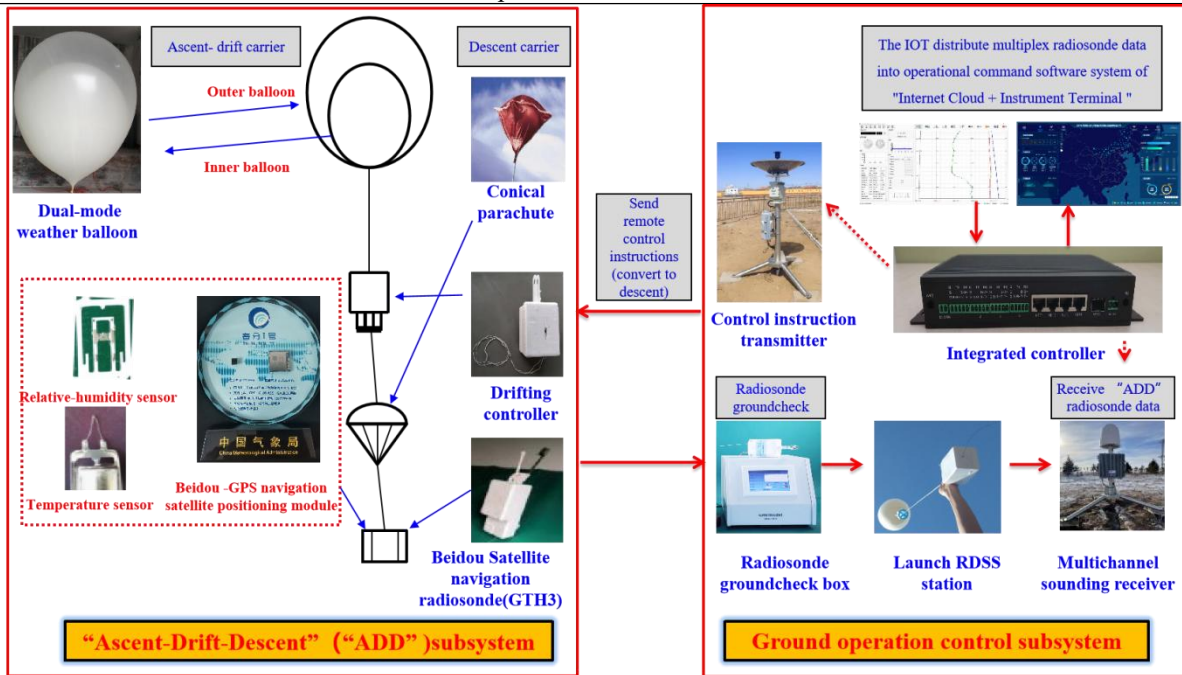


94
 95 **Figure 1. Operational principle diagram of the Ascent-Drift-Descent Radiosonde System (ADDRS).**

96 **Table 1. Main instruments and key functions of ADDRS.**

No	Subsystem	Instruments	Key Function
1	'ADD' subsystem	dual-mode balloon	'outer balloon' as ascent carrier, 'inner balloon' as drift carrier
2		parachute	parachute as the carrier of the descent phase
3		drifting controller	Adaptive control of drift and descent
4		radiosonde	The temperature, pressure, humidity, wind measurement meet the demand for long-term stratospheric observation

5	Ground station	ground inspection ground check, balloon inflation, launch, and other tasks before the equipment is launched
6	Multichannel sounding receiver	8 channels receive radiosonde data simultaneously
7	Ground operation control subsystem	In the weather-sensitive area without a station, the active fusing drifting controller is carried out and the descent measurement is started
8	operational management system	Real-time acquisition, transmission, quality control, and timely delivery of control instructions for ADDRS data, providing real-time high-quality data to weather analysis and numerical prediction models



97

98

Figure 2. Schematic representation of the equipment composition for ADDRS.

99

100

101

102

103

104

105

106

107

108

109

The ADDRS primarily consists of the 'ADD' subsystem and the ground operational control subsystem, as shown in Table 1 and Fig. 2. The 'ADD' subsystem encompasses a dual-mode balloon with a parachute, a drifting controller, and a radiosonde. The dual-mode balloon features a design where one balloon embedded within another, both made from a latex material similar to that of operational meteorological sounding balloons and filled with hydrogen. Upon inflation and launch of the dual-mode balloon, the 'ADD' subsystem at a rate of ascent between 5 and 7 m/s (WMO-No. 8., 2025). As it rises, the external air pressure decreases, causing the balloon to expand. At the predetermined altitude (generally between 28km and 30km), the outer balloon bursts due to its expanding volume, marking the conclusion of the ascent phase measurement. Given that the outer balloon bursts within the stratosphere, where vertical air movement is minimal, horizontal movement becomes predominant. The inner balloon enable it to resist bursting. And the buoyancy of the inner balloon attains equilibrium with vertical stability, starting the drift phase.

110

111

112

113

114

After drifting for a predefined duration, which may vary from a couple of hours to over ten hours, the drifting controller separates the inner balloon from the rest of the ADDRS equipment, thereby terminating the drift phase. Meanwhile, the remaining components—comprising the parachute and radiosonde—begins to descend. The parachute is promptly deployed, facilitating the radiosonde in collecting data during the descent phase, while acting as its carrier. This descent persists until the equipment touches down, thereby completing the

115 final phase of the 'ADD' process. At this point, ADDRS has successfully completed the three-phase 'Ascent-
116 Drift-Descent' measurement.

117 The ground operation control subsystem of ADDRS comprises four main components, including the
118 balloon launch station, ground data-receiver (downlink communication), control command transmitter (uplink
119 communication), and the operational management system. The balloon launch station is similar to existing
120 meteorological radiosonde launch station, undertaking tasks such as ground checks, balloon inflation, and
121 launching the balloon with a radiosonde at scheduled intervals. Ground data-receiver can also be placed at the
122 balloon launch station. However, its layout and function differ from the operational-ground data-receiver. Due
123 to the ADDRS drift phase, the horizontal distance between the descent point of the radiosonde and its launch
124 point can exceed 500km, while operational radiosonde data reception has a maximum linear transmission
125 distance of around 200km-300km. Therefore, the traditional single-station, point-to-point radio communication
126 mode of radiosondes is inadequate for ADDRS data reception. Thus, the ground to upper-air communication
127 system has been upgraded from point-to-point to a multiple-to-multiple model. In areas through which the
128 radiosonde's ADD phases may pass, ground data-receivers are strategically deployed. This configuration enables
129 multiple ground data-receivers to concurrently receive data from a single radiosonde or alternatively, a single
130 receiver to capture data signals from several radiosondes simultaneously. Consequently, the ground data-
131 receiver is designed as a P-band 8-channel parallel data receiver, capable of receiving data from multiple
132 radiosondes simultaneously. Additionally, control command transmitters are located at the ground station and
133 other locations. These transmitters send control instructions from the ground to the drifting controller in the
134 air through uplink communication. This system allows for the adjustment of the drift phase elevation,
135 termination of the drift phase, and switching to the descent phase measurement as needed.

136 The operational management system acts as the brain of the entire ADDRS system. Multiple ground data-
137 receivers and control command transmitters are connected to the operational management system by the Internet.
138 These ground data-receivers continuously transmit data to the operational management system in real-time for
139 processing, display, and storage. Based on the ADDRS trajectory and specific weather and climate conditions,
140 comprehensive decision-making allows the operational management system to transmit control instructions to
141 control command transmitters which then relay them to the drifting controller in the air to execute the desired
142 functions.

143 The 'Internet cloud + Instruments terminal' architecture enables real-time, efficient, and bidirectional
144 communication across the entire network during the 'ADD' phases. This configuration supports the seamless
145 real-time acquisition, transmission, and quality control of ADDRS data while ensuring rapid data delivery for
146 weather forecasting. Consequently, it enhances the timeliness and availability of radiosonde data for forecasting
147 purposes.

148 **3. Critical scientific problems**

149 **3.1. Carrier technology**

150 **3.1.1 Study on the influence of atmospheric environment on the net lift power of balloons**

151 A multitude of meteorological factors, encompassing air temperature, air pressure, solar radiation, and
152 other external environmental conditions, coupled with the gas volume of the outer balloon directly influences

153 its net lift and burst altitude. Variations in air pressure and temperature within the outer balloon, induced by
 154 external meteorological conditions, interact with the expansion dynamics of the inner balloon. These factors, in
 155 conjunction with the optimum volume of the inner balloon, collectively influence the altitude during the drift
 156 phase and the static equilibrium of the inner balloon. Consequently, controlling the hydrogen inflation volume in
 157 the dual-mode balloon presents a significant challenge.

158 The ADDRS research team conducted an in-depth theoretical analysis of the ascent and drift processes of
 159 the dual-mode balloon, focusing on three areas: upper atmosphere model expansion, the balloon's dynamic
 160 equation, and a thermodynamic model. This study led to the development of a coupling model that accounts for
 161 the effects of atmospheric conditions on the balloon's net lift (from now on referred to as the 'coupling model')
 162 (Liu, S. J et al., 2022). This model provides a theoretical foundation for determining the net lift force, ascent
 163 velocity, and target burst altitude of the dual-mode balloon, enabling precise control of the mass of air in the
 164 balloons in the dual-mode balloon under varying meteorological conditions.

165 **Table 2. Inflate test results based on coupling model.**

Inflatable mode	Effective launch times	Drift number of times	Drift success rate	$\geq 4h$ number of times	$\geq 4h$ success rate
Algorithm software	611	479	78.40%	436	71.36%

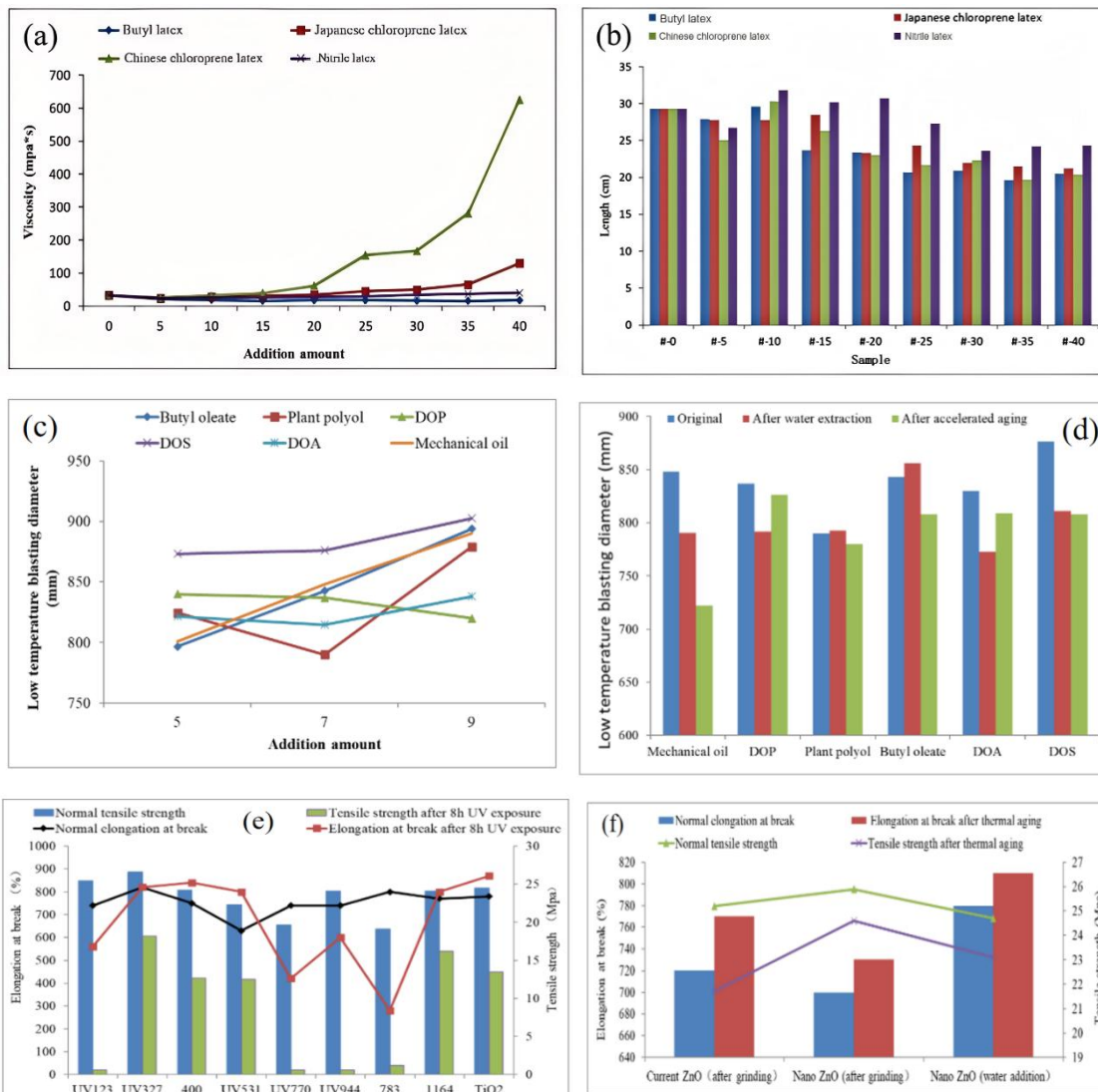
166 Table 2 presents data from six stations (Changsha, Wuhan, Anqing, Yichang, Nanchang, and
 167 Ganzhou) situated along the middle and lower reaches of the Yangtze River in 2021. And based on the
 168 sounding balloon observation data in Guangdong from August 2022 to October 2023, the optimum volume
 169 capacities of related factors of the inner and outer balloons of the dual-mode sounding balloon on the success
 170 rate of the drift were studied, and a reasonable inflation scheme was established to improve the success rate of
 171 the drift. The research shows that the theoretical inflation amount of the inner balloon for drifting at the
 172 expected height is 55.6 mol. Affected by day and night conditions, the inflation amount during the day should be
 173 controlled at 52.6 ± 2 mol, and at night, it should be controlled at 57.6 ± 2 mol. The burst height of the outer
 174 balloon has a significant impact on the success rate of the drift. When the burst height of the outer balloon is
 175 within the expected height, the success rate of the drift can reach 82%. The success rate of the drift during the
 176 day is higher than that at night, and the success rate under clear sky conditions is higher than that under cloudy
 177 and rainy conditions. Under rainy conditions, the success rate of the drift is only 50.2%. After verification, the
 178 success rate of the drift can reach 93.5% by adopting the reasonable inflation scheme (Xu et al., 2025).

179 3.1.2 Performance improvement of the double - layer balloon

180 The ascent phase of meteorological sounding typically lasts between 1.5 and 2 hours. However, during the
 181 ADD process, the inner balloon of the dual-mode balloon is exposed to low temperatures, intense ultraviolet
 182 radiation, and high ozone concentrations for several hours or even up to ten hours. To address these challenges,
 183 the ADDRS research team conducted formulation tests to enhance the inner balloon resistance to these
 184 environmental factors, with a particular emphasis on natural latex modification, cold resistance, and anti-aging
 185 systems. Considering that latex hot air aging performance improves air tightness and balloons are exposed to
 186 prolonged sun exposure and hydrogen loss, the incorporation of a specific latex compound was found to
 187 augment durability. Fig. 3a and 3b show that the addition of latex formulas had minimal impact on the latex

188 viscosity and the balloon appearance while improving its tensile strength and thermal aging resistance. Fig. 3c
 189 and 3d demonstrate that butyl oleate exhibits the lowest reduction in low-temperature burst performance after
 190 water extraction and accelerated aging, making it the best-performing cold-resistant agent. Consequently, this
 191 agent was integrated into the formula to bolster cold resistance. For the anti-aging system, illustrated in Fig.3e
 192 and 3f, nano zinc oxide, which can be diluted directly with water to replace traditional zinc oxide, was used.
 193 Additionally, we incorporated antioxidants to enhance the balloons' resistance against ultraviolet and ozone
 194 degradation. These formula improvements extend the inner balloon lifespan under harsh conditions of low
 195 temperature, intense UV radiation, and high ozone levels. This enhanced durability has been applied to the inner
 196 balloon, resulting in an extended service life and a high success rate during the drift phase (Zhu et al., 2021;
 197 Shen et al., 2020).

198



199

200

201 **Figure 3. Modification test of natural latex in the inner sphere:** (a) Four types of modified natural latex materials—
 202 Butyl latex, Japanese chloroprene latex, Chinese chloroprene latex, and Nitrile latex—were screened and added to
 203 natural latex using the homogenization method. (b) Physical properties of the modified natural latex pellet samples
 204 were evaluated for operational and thermal aging tensile testing. (c) Butyl oleate, Plant polyol, DiOctyl Phthalate
 205 (DOP), DiOctyl Sebacate (DOS), DiOctyl Adipate (DOA), and mechanical oil were added to natural latex as cold
 206 resistance agents. Cold resistance system test: The blasting diameters of six types of cold-resistant samples were tested
 207 using low-temperature blasting instruments at -85°C. (d) Low-temperature blasting diameters were measured for six
 208 types of raw, water-pumped, and aged samples with seven parts of cold-resistant agents added. Anti-aging system test:
 209 (e) Comparison of tensile properties among nine anti-aging agents—UV327, UV400, UV531, UV1164, and TiO2

210 filler—with 0.2 parts of one-component anti-aging agent after eight hours of operational and ultraviolet aging. (f)
211 Comparison of tensile properties after ozone aging between Nano ZnO and ZnO.

212 3.2 Payload technology

213 3.2.1 Performance improvement of the radiosonde

214 The ADDRS payload unlike operational radiosonde, ADDRS operates effectively across all three phases of
215 the ADD process, requiring a minimum operational time of six hours. This extended operation necessitates a
216 larger-capacity battery for the ADDRS radiosonde. Additionally, the radiosonde's weight affects the balloon's
217 inflation volume, making it essential to reduce the radiosonde's weight where possible. Therefore, an integrated,
218 lightweight, and low-power radiosonde is crucial, and the ADDRS research team developed a specialized SoC
219 (System on Chip) module (named Equinox I) for CMA's GTH type of Beidou-based radiosonde.

220 The GTH3 employs a specialized SoC module of meteorological sounding and utilizes a multi-layer board
221 design and miniaturized components to reduce the size, weight, and power consumption. Besides GTH3
222 radiosonde compare to GTS12 radiosonde of L-band Secondary Wind-sounding radar (Chinese operational
223 radiosonde before 2025) significantly reducing the overall size, weight, and power consumption of the device.
224 Furthermore, the amount of plastic and toxic materials in the circuit boards has also been substantially reduced
225 (Table 3).

226 The GTS12 and GTH3 radiosonde use the same PTU sensor, P(MEMS piezo-resistive), T(adopting self-
227 developed NTC bead thermistor (reducing from diameter $\leq 1\text{mm}$ to $\leq 0.4\text{mm}$) volume reduction, higher
228 sensitivity), U (capacitive thin-film polymer humidity sensor). The difference lies in that 'Instrumentation and
229 Methods' :

230 For P [Design the temperature compensation circuit and establish the correction equation by fitting the
231 sensor characteristic surface through multiple temperature segments and multiple pressure points to achieve
232 higher measurement accuracy.]

233 For T [Optimize the installation structure, included Angle and lead length through simulation analysis, and
234 effectively reduce the influence of solar radiation by improving the installation structure and coating process.]

235 For U [Optimize the Temperature compensation Correction Algorithm and humidity hysteresis Correction
236 Algorithm for Humidity sensors]

237 The GTH3 participated in WMO UAI2022 (Upper-Air Instrument Intercomparison Campaign organized
238 by the World Meteorological Organization (WMO) and co-organized by the Deutscher Wetterdienst (DWD) in
239 2022) with the results shown in Table 4. It is suitable for applications in ORUC(Operational and Research Use
240 in Climatology), including aeronautic meteorology, near/ultra-short-term forecasting, global numerical weather
241 prediction, and real-time monitoring (WMO IOM-143., 2024).

Table 3. Comparison of parameters among RS41, GTH3 and GTS12 radiosonde.

Radiosonde type	Positioning method	Volume (mm ³)	Weight (g)	Transmitting power (mW)	Working time (min)	Data Transmission Rate(bps)	Battery Weight (g)	Foam Packaging Weight (g)	Circuit boards Weight (g)
GTS12 radiosonde	Radar positioning	190×90×245	<400	400≤	>120	1200	<250	<70	<80
GTH3	Equinox I	155×65×60	<120(for one profile)	100≤	>240	Optional,2400,4800,9600	<40	<30	<50
		155×65×60	<170(for “ADD” three phase profile)	100≤	>640		<90	<30	<50
Vaisala RS41	u-blox G7020	155×60×46	109	60	>240	4800	76	/	/

243 Table 4. The evaluation results of GTH3 radiosonde temperature, pressure, relative humidity, wind and geopotential height in WMO Instruments and Observation Methods Report
244 No. 143, page.150(Note: The data are in the form of $\Lambda_{c,L} \delta_{c,L} \pm \epsilon_{c,L}$, where $\Lambda_{c,L}$ represents the individual measurement root mean square error, $\epsilon_{c,L}$ denotes the measurement
245 uncertainty, $\delta_{c,L}$ is the measurement error, and $\sigma(\delta)$ indicates the measurement standard deviation. The planetary boundary layer (PBL) ranges from surface to 2 kilometers; the
246 free troposphere (FT) ranges from 2 kilometers to the tropopause 12 kilometers are in the ; the upper troposphere/lower stratosphere (UTLS) ranges from 7 kilometers to 17
247 kilometers; the middle and upper stratosphere (MUS) is above 17 kilometers up to the bursting point of the sounding balloon.)
248

Time	Height	Atmospheric temperature [K]	Relative humidity [%RH]	Geopotential height [m]	Pressure [hPa]	Wind (horizontal)direction[°]	Wind (horizontal)speed [m.s ⁻¹]	Wind (horizontal)vector [m.s ⁻¹]
Day	PBL	$0.18_{0.17}^{+0.05} \pm 0.03$	$7.00_{4.41}^{-5.43} \pm 0.74$	X	X	X	X	X
	FT	$0.12_{0.11}^{+0.05} \pm 0.04$	$8.75_{8.02}^{-3.50} \pm 0.60$	$5.9_{5.5}^{+2.0} \pm 1.8$	$0.4_{0.4}^{-0.0} \pm 0.1$	$3.6_{3.6}^{-0.4} \pm 0.2$	$0.2_{0.2}^{-0.0} \pm 0.0$	$0.3_{0.1}^{+0.2} \pm 0.0$
	UTLS	$0.09_{0.08}^{+0.01} \pm 0.03$	$7.73_{7.58}^{-1.55} \pm 0.40$	$13.2_{8.6}^{+10.0} \pm 3.8$	$0.4_{0.2}^{-0.3} \pm 0.1$	$2.5_{2.5}^{-0.2} \pm 0.3$	$0.2_{0.2}^{-0.0} \pm 0.0$	$0.3_{0.2}^{+0.2} \pm 0.0$
	MUS	$0.27_{0.16}^{+0.22} \pm 0.10$	$1.69_{0.82}^{+1.48} \pm 0.46$	$29.5_{17.9}^{+23.4} \pm 4.2$	$0.3_{0.1}^{-0.2} \pm 0.0$	$6.1_{6.1}^{-0.4} \pm 0.2$	$1.3_{1.3}^{-0.0} \pm 0.0$	$1.5_{1.5}^{+0.3} \pm 0.0$
Night	PBL	$0.38_{0.34}^{-0.18} \pm 0.05$	$4.72_{4.66}^{+0.74} \pm 0.15$	X	X	X	X	X
	FT	$0.15_{0.15}^{+0.02} \pm 0.02$	$6.41_{6.03}^{+2.16} \pm 0.11$	$5.8_{5.8}^{+0.4} \pm 0.4$	$0.5_{0.5}^{+0.1} \pm 0.2$	$2.6_{2.6}^{-0.2} \pm 0.2$	$0.2_{0.2}^{-0.0} \pm 0.0$	$0.2_{0.1}^{+0.2} \pm 0.0$
	UTLS	$0.12_{0.10}^{+0.06} \pm 0.05$	$6.82_{5.74}^{+3.70} \pm 0.26$	$11.5_{8.6}^{+7.7} \pm 3.4$	$0.3_{0.2}^{-0.1} \pm 0.1$	$2.4_{2.4}^{-0.1} \pm 0.1$	$0.2_{0.2}^{-0.0} \pm 0.0$	$0.2_{0.1}^{+0.2} \pm 0.0$
	MUS	$0.10_{0.10}^{+0.03} \pm 0.02$	$1.71_{0.74}^{+1.54} \pm 0.28$	$26.7_{16.8}^{+20.7} \pm 4.2$	$0.1_{0.1}^{-0.1} \pm 0.0$	$4.5_{4.4}^{-0.6} \pm 0.2$	$0.2_{0.2}^{-0.0} \pm 0.0$	$0.4_{0.3}^{+0.3} \pm 0.0$

250 **3.2.2 Drifting controller**

251 The drifting controller can be considered part of the ADDRDS payload. It connects to an inner balloon above
252 and a parachute and radiosonde below. The controller fuses a wire with an instant high electric current,
253 triggering the mechanical device to disconnect the parachute and the radiosonde. The controller serves two main
254 functions during the drift phase:

- 255 1. Similar to the Windborne system, it is equipped with a ballast-dropping mechanism to control its weight,
256 allowing the inner balloon to better adapt to changes in altitude.
- 257 2. Separate the inner balloon from the other sounding equipment (parachute and radiosonde). Moreover, the
258 drifting controller can also initiate the fuse based on predetermined control rules, such as altitude limits
259 (≤ 18 km), specified time, the latitude and longitude of a designated area, or upon receiving commands
260 from the ground. This action can be taken before the drifting balloon is about to enter the specified area or
261 approach the maximum drift height. As a result, it will effectively end the drift phase, separating the
262 parachute and radiosonde from the balloon.

263 **3.3. Receiving radiosonde data and sending control instructions technology**

264 The ADDRDS ground data-receiver utilizes a high-gain, low-power, ultra-compact omnidirectional antenna,
265 along with super-heterodyne architecture and multiple communication protocol algorithms, including time
266 division multiple access, frequency division multiple access, and code division multiple access (Gong et al.,
267 2021). It supports various frequency modulation modes and achieves a receiving sensitivity of better than -120
268 dBm (at 2400 bps), effectively addressing self-interference issues in multi-channel radiosonde data reception.
269 Additionally, the system incorporates narrow-band wireless communication technology to improve low-
270 elevation reception when the radiosonde drops below the receiving antenna's height, facilitating broad-area
271 coverage with a visual range radius for upper-air coverage of at least 200 km. The receiver can adapt to diverse
272 application scenarios, such as fixed stations, vehicles, and ships. With an average data reception rate of 99.7%,
273 the ground receiver at the Anqing station has demonstrated an impressive maximum reception distance of up to
274 487 km.

275 Unlike the one-way (downlink) communication mode used in operational sounding systems, the ADDRDS
276 control command transmitter can send ground instructions to the drifting controller, with a linear
277 communication range extending beyond 300 km. This capability allows for precise control over the drifting
278 controller to execute actions such as releasing counterweights or separating the balloon from the parachute and
279 radiosonde, enabling the radiosonde to conduct drift phase measurements within the target area (Liu et al., 2021).
280 During field tests, over ten balloon discharge control commands were successfully transmitted, with the farthest
281 reaching 403 km.

282 **3.4. 'ADD' measurement technology**

283 The details of the ADD measurement method are outlined by (Cao et al., 2019). The ascent phase
284 measurement technique adheres to the guidelines outlined in the CMA technical specification. The primary
285 research focus of the ADDRDS is on the measurement techniques for the drift and descent phases.

286 **3.4.1 Temperature measurement method in the flat drift phase**

287 During the drift phase of ADDRS, the inner sphere of the dual-mode balloon moves with the horizontal
288 airflow in the stratosphere. The radiosonde's vertical movement, with the surrounding atmosphere, is minimal
289 and can be approximately considered as drifting with the horizontal wind. The effect of radiation on the
290 temperature sensor during this phase is greater than during the ascent and descent phases, leading to
291 considerable measurement errors that are challenging to correct using general quality control algorithms.

292 Given the unique conditions of stratospheric air temperature measurement, the ADDRS research team
293 employs a multi-physical field, fluid-structure coupled computational fluid dynamics (CFD) approach to model
294 the behavior of the temperature sensor in high-altitude, low-wind-speed environments. This model calculates the
295 flow and the temperature field, accounting for radiation effects based on sun elevation, ventilation, sensor size,
296 and surface reflectivity. To ensure broad applicability, neural networks, and other mathematical methods are
297 used to fit the extensive simulation data, yielding practical error-correction equations (Yang et al., 2014).

298 Considering that there may be discrepancies between CFD simulations and real environmental conditions,
299 the ADDRS research team uses instruments such as low-pressure wind tunnels and solar simulators to create an
300 experimental platform. This setup simulates ventilation, air density, and solar radiation conditions during the
301 drift phase, allowing for the measurement of temperature errors due to solar radiation. These measurements
302 verify and refine the simulation-based error correction equations (Yang et al., 2022).

303 **3.4.2 Vertical wind data during the parachute descent**

304 Currently, due to the pendulum effect, vertical wind measurements cannot be performed in balloon-borne
305 soundings. The parachute-drop wind measurement model established by the WMO and NCAR does not address
306 vertical wind measurement directly (Wang et al., 2015), instead assuming a zero vertical wind speed. This
307 model assumes that the parachute-drop system is influenced only by gravity and vertical resistance, omitting
308 other factors like buoyancy, additional forces, and parachute rotation during descent. This limitation prevents
309 the analysis of vertical wind and also affects the accuracy of horizontal wind field calculations (Jensen et al.,
310 2010; Ingleby et al., 2022).

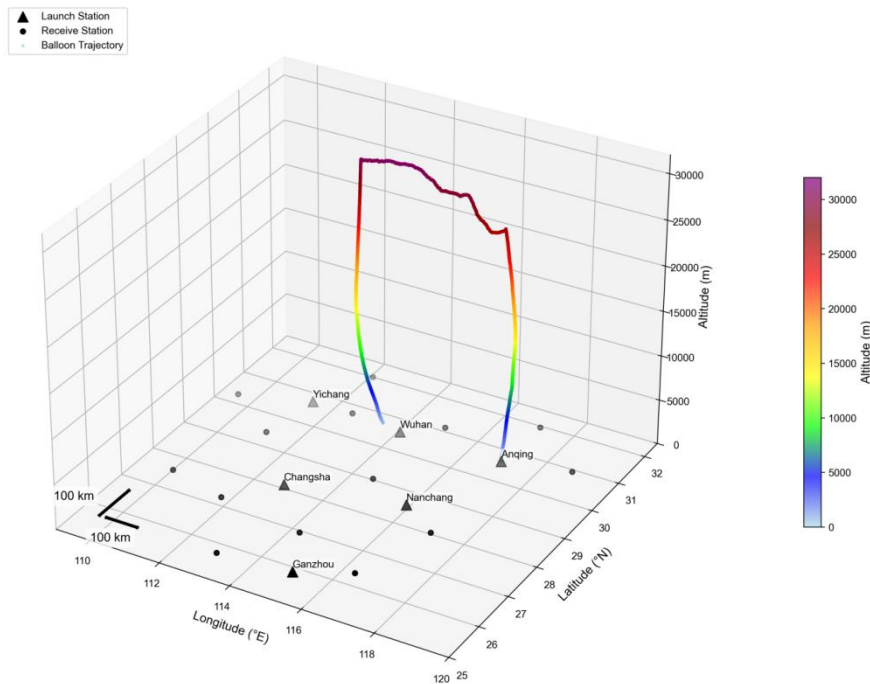
311 Therefore, the ADDRS research team developed a more comprehensive vertical wind measurement model
312 by considering all relevant forces acting on the balloon-launched and parachute descent dropsonde system,
313 utilizing the domestic Beidou-based radiosonde, shows significant promise. The Beidou-based radiosonde
314 demonstrated acceptable accuracy during both ascent and descent phases compared to the RS92 standard. The
315 key advantages identified were the ability to temporally intensive sounding observations (effectively obtaining
316 an 'ascent' and 'descent' profile from one launch) and the potential to spatially expand coverage through the drift
317 of the parachute, allowing for a 'one-station launch, multi-station reception' model. This technology aligns with
318 the trend towards automated, quantitative remote sensing in meteorological observation (Guo et al., 2018).
319 Comparative tests led to the selection of conical parachutes to minimize swing effects on measurements. The
320 string length between the balloon/parachute and the GTH3 radiosonde is standardized at 30 meters in manual
321 launches. This length helps reduce sensor exposure to balloon wake effects but amplifies pendulum motion in
322 wind data. And carried out more than ten comparative tests for the selection of conical parachutes. The
323 oscillation angle of conical parachute is less than 1° , which can ensure the rationality of the Gaussian filtering
324 correction filter window for the horizontal wind in the descent phase. Meanwhile, a larger main parachute size
325 can reduce the descent speed. Therefore, without considering the cost, a 'large conical parachute' is

326 recommended for the descent phase detection of ADDRS. And make sure the parachute area is tailored to match
 327 the radiosonde weight. The descent phase of ADDRS could achieve a low-level descent speed of $6 \text{ m/s} \pm 1 \text{ m/s}$
 328 can be achieved in UTLS (upper troposphere and lower stratosphere (7-17km), and a swing angle below 5° , as
 329 well as a vertical wind measurement uncertainty of less than 1 m/s . These findings demonstrate that the model is
 330 effective for calculating vertical wind.

331 4. Field experiments and data quality verification

332 4.1. Field experiment in the middle and lower reaches of the Yangtze River Region

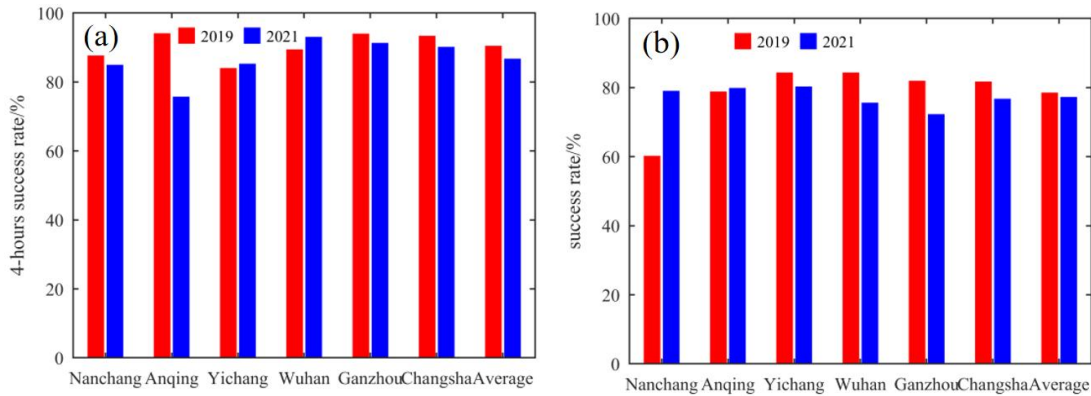
333 From 2019 to 2021, ADDRS conducted field tests and application research across a wide area in the middle
 334 and lower reaches of the Yangtze River in China. The research focused on measurement data processing
 335 methods, quality control algorithms, and application technologies across diverse scenarios. The ADDRS
 336 radiosondes were launched from six stations. They were Anqing, Wuhan, Yichang, Nanchang, Changsha, and
 337 Ganzhou, which located in Anhui, Hubei, Jiangxi, and Hunan provinces. A total of 14 ground radiosonde data
 338 receivers were strategically positioned around these six stations, spaced approximately 150 km apart. The test
 339 covered an area of 600,000 square kilometers, as shown in Fig. 4, and show a trajectory for ADDRS at the
 340 Anqing station at 12:00 UTC on 11 July 2021.



341
 342 **Figure 4. The network distribution of ADDRS and an example of measurement: the trajectory for ADDRS at the**
 343 **Anqing station at 12:00 UTC on 11 July 2021. The black triangles represent balloon launch stations of ADDRS , while**
 344 **the black dots represent receive radiosonde data stations of ADDRS.**

345 During the 13-month experimental period, 3,177 ADDRS launches were conducted, with 3,012 classified
 346 as effective launches, of which 2,369 achieved successful drifting. Among these, 2,136 launches resulted in
 347 drifting for more than 4 hours. The overall drifting success rate was 79%, with a 4-hour drifting success rate of
 348 71% (Fig. 5).

349

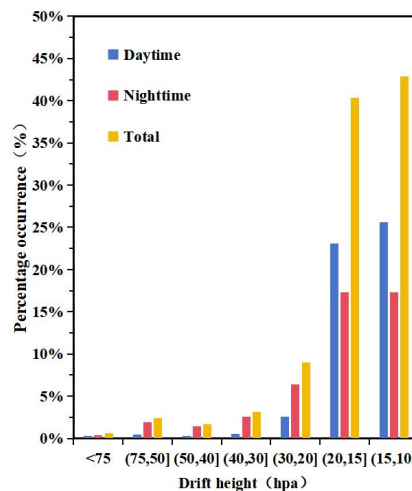


350

351 **Figure 5. The field experiment in the middle and lower reaches of the Yangtze River Region (2019-2021): (a) Drifting**
 352 **success rate; (b) 4-hour drifting success rate.**

353 From March to September 2021, 2,427 'ADD' radiosonde launches were conducted, with 2,281 classified
 354 as effective launches, of which 1,772 achieved successful drifting. Among these, 1587 launches resulted in
 355 drifting for more than 4 hours. The overall drifting success rate was 78%, with a 4-hour drifting success rate of
 356 70%. The 1,772 successful drifts were analyzed (Fig. 6), and 937 were successful during the daytime,
 357 accounting for 53%. The successful nighttime drifting was 835 times, accounting for 47%, somewhat worse
 358 than the daytime performance. The drift heights ranging from < 75hPa (<18km) to 15hPa-10hPa (28km-32km)
 359 were statistically analyzed. The proportion of outer balloon explosion heights within 15hPa-10hPa (28km-32km)
 360 was the largest (43%). And the proportion of 20hPa-15hPa (26km-28km) is 40%, the proportion of 30hPa-
 361 20hPa (24km-26km) is 9%, and the total proportion of beyond 30hPa is 92%. Therefore, The drift height meets
 362 the GBON requirement of attaining at least 30hPa for a majority of ascents, with a subset of ascents also
 363 reaching the 10hPa level (WMO, 2020).

364

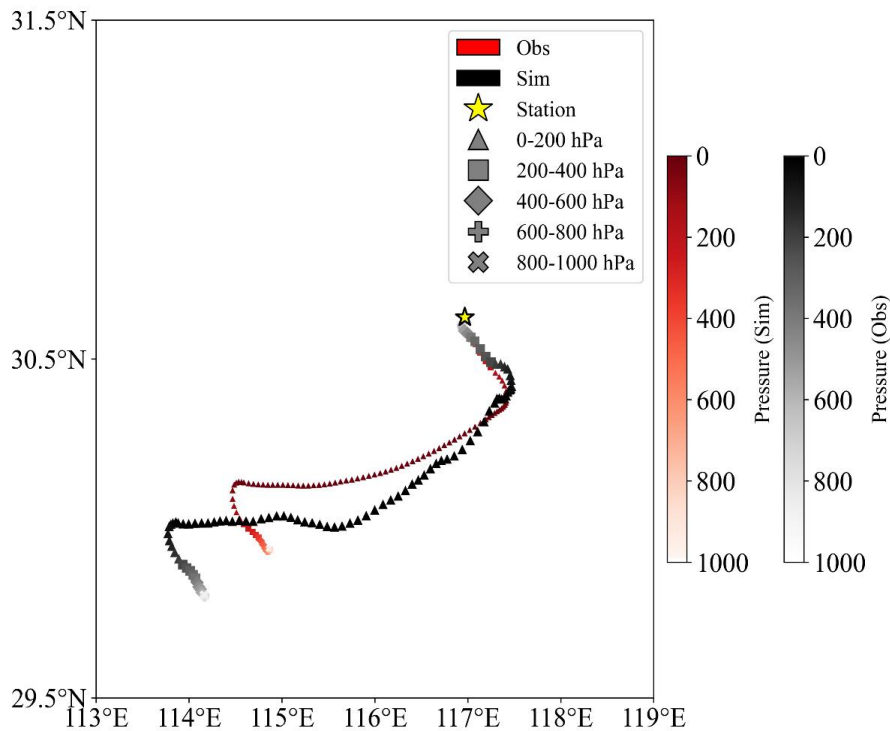


365

366 **Figure 6. The sounding-forecasting interactive network experiment (2021): (a) drifting height; (b) descent height.**

367 Due to the limited availability of high frequency, continuous measurement data for the stratospheric
 368 atmosphere, experiments were conducted in the middle and lower reaches of the Yangtze River to obtain direct
 369 measurement data with high spatial and temporal density (Zhang et al., 2021). The simulated and observed

370 trajectories are represented by red and black, respectively (Fig. 7). A color gradient based on pressure altitude is
 371 used to indicate the variation of trajectory height along the path.



372

373 **Figure 7. Schematic diagram of the observed (black) and simulated (red) trajectories. The yellow pentagram**
 374 **indicates the radiosonde station. The color of each point represents the corresponding pressure level. Distinct**
 375 **markers are used every 200hPa to enhance visual differentiation.**

376 The balloons drifting of ADDRS radiosondes data in the above troposphere have been very useful for
 377 verification FY-3D satellite temperature and humidity profiles (Zhou et al., 2023; Zhou et al., 2024). And
 378 application in observing certain features of gravity waves in the lower stratosphere (He et al., 2024; Yang et al.,
 379 2021) and feature extraction and analysis of atmospheric turbulence (Yang et al., 2023).

380 4.2 Data quality evaluation

381 Aiming at the characteristics of high-resolution ADDRS data for quantitative application, the ADDRS
 382 research team carefully evaluated ADDRS data using 31 data quality control methods based on the guidelines
 383 for CMA technical specification of operational upper-air meteorological observation (Wang, D et al. 2020). For
 384 the data quality of the ascent phase of the ADD radiosonde, refer to the results in Table 4. Additionally, the
 385 fifth generation of ECMWF (ERA5) global reanalysis (Hersbach et al., 2020) was used to evaluate the quality of
 386 four upper-air radiosonde observations stations' ADDRS data in Guangdong (Zhang, C.Z et al., 2025), and
 387 Table 5 shows the results of field experiment in the middle and lower reaches of the Yangtze River Region (Yao
 388 et al., 2026). The standard deviation results of ascent phase compared with descent phase (temperature, u-wind,
 389 v-wind) show good consistency. The conclusion is basically consistent with the results of Table 4.

390 But for relative humidity (RH), different radiosonde manufacturers may adopt distinct saturation vapour
 391 pressure (SVP) equations in calibrating humidity sensors. This difference in the choice of SVP equation can lead

392 to discrepancies in relative humidity measurements among different radiosonde types, especially under low-
 393 temperature conditions.

394 The ADDRS radiosonde humidity sensor is calibrated using the Goff (1957) SVP equation recommended
 395 in earlier WMO publications (WMO, 2012). Moreover, relative humidity from the ERA5 dataset is calculated
 396 using the Buck SVP equation. To ensure a more consistent comparison, relative humidity was recalculated from
 397 temperature and specific humidity in the ERA5 dataset using the Goff (1957) SVP equation, with the SVP
 398 assumed over liquid water only. The results show that the O–A bias and RMSE of relative humidity under low-
 399 temperature conditions are reduced and become much more physically reasonable.

400 We also note that the discrepancies between the measured wind and temperature data during the drift phase
 401 and the ERA5 reanalysis data are significantly larger, a phenomenon consistent with most radiosonde data
 402 comparisons at high altitudes (typically above 300hPa) against ERA5 (Liu, B et al., 2021). With the continued
 403 accumulation of continuous drift phase of ADDRS data in the future, it holds the potential to support research
 404 and improvements in reanalysis datasets like ERA5. And (Ingleby et al., 2022) noted that ECMWF's operational
 405 system excludes descent temperatures above 150hPa during assimilation due to these biases. This conservative
 406 approach ensures that only reliable data are used, while further research continues to refine bias corrections.the
 407 temperature 'descent' warm results represents a noteworthy issue for future research.

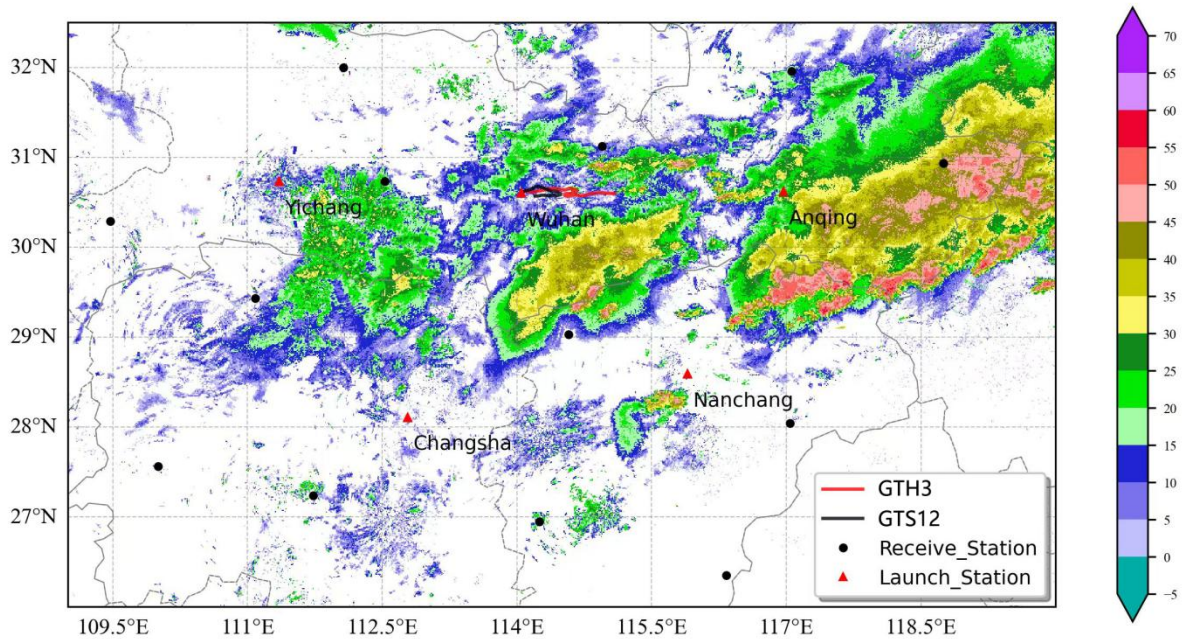
408 **Table 5. Comparative analysis of after-quality control of ADDRS radiosonde data and ERA5.**

			U (m/s)		V (m/s)		T (K)		RH (% RH)	
			bias	std	bias	std	bias	std	bias	std
Ascent	Day	Above troposphere	0.03	1.73	0.11	1.91	-0.4	1.04	/	/
		Below troposphere	0.13	1.41	0.08	1.47	0.04	0.69	1.32	8.57
	Night	Above troposphere	-0.02	1.72	-0.01	1.87	0.01	1.02	/	/
		Below troposphere	0.13	1.4	0.02	1.46	0.08	0.66	1.62	8.32
Drift		Above troposphere	/	3.32	/	3.22	/	3.09	/	/
Descent	Day	Above troposphere	0.16	1.74	-0.02	1.9	0.9	1.14	/	/
		Below troposphere	0.14	1.65	0.01	1.7	0.42	0.75	-1.7	10.12
	Night	Above troposphere	0.16	1.73	0.03	1.84	0.21	1.06	/	/
		Below troposphere	0.15	1.67	0.05	1.67	0.04	0.73	0.5	10.47

409 **5. Application of ADDRS in numerical forecasting techniques**

410 **5.1 A case study of weather analysis**

411 Through long-term testing, the ADDRS have the potential for capture key information in convective
 412 system monitoring. From July 8 to 9, 2021, a strong convective weather event with a long duration and a large
 413 impact area occurred in the middle and lower reaches of the Yangtze River in China. Convection developed and
 414 moved to northern Jiangxi, northern Zhejiang, southern Anhui, and southern Jiangsu overnight on July 8 (Fig.8).
 415 The drifting trajectories of ADDRS radiosondes were from west to east, which aligned with the movement and
 416 development direction of severe convection. The descent phase radiosondes of ADDRS provides effective
 417 monitoring and insights in track the occurrence of the convective system and the changes in the ambient field.

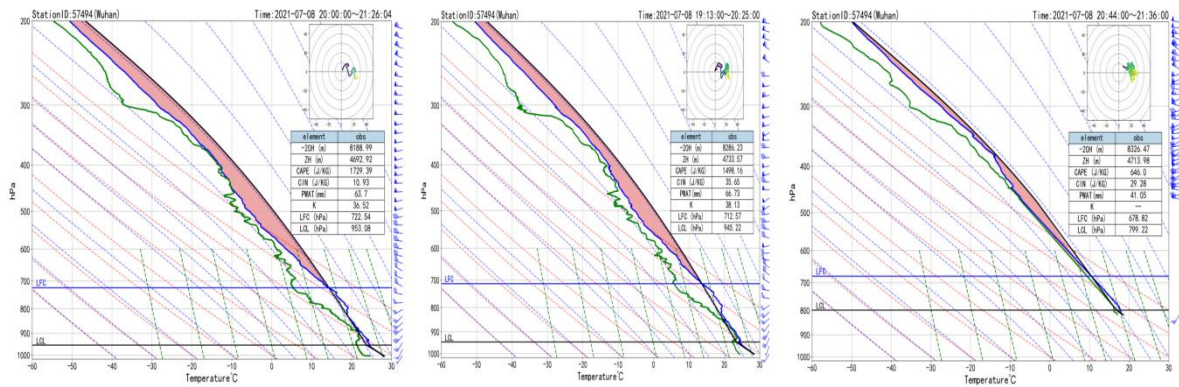


418

419 **Figure.8 The trajectory for GTH3 and GTS12 radiosonde at the Wuhan station and radar reflectivity image at 12:00**
 420 **UTC on 8 July 2021.**

421 Figure 8 displays the trajectory data of the ADDR5 and GTS12 radiosondes launched from the Wuhan
 422 Meteorological Station. On the night of 8 November, at 11:15 UTC, Wuhan was situated on the western flank of
 423 the main convective system. The ADDR5 radiosonde was launched at this time from the station, followed by the
 424 GTS12 radiosonde at 12:00 UTC from the same location. During the ascent phase, the curve of the ADDR5
 425 radiosonde (Fig. 9b) exhibited a trend similar to that of the GTS12 (Fig. 9a). A comparison of the ascent-phase
 426 data revealed that the convective available potential energy (CAPE) values differed between the two instruments
 427 as convection developed. The GTS12 measured a CAPE of 1729.39 J/kg at 12:00 UTC, higher than the value of
 428 1498.16 J/kg recorded by the ADDR5 at 11:15 UTC.

429 Influenced by an upper-level westerly jet, the ADDR5 sounding balloon drifted eastward toward the
 430 Wuhan. At 13:30 UTC, ADDR5 conducted descent phase measurements (Fig. 9c). As shown in the layer curve,
 431 the CAPE value at 21:30 decreased compared with that at 12:00 UTC, dropping to 646.0J/kg, which was lower
 432 than the energy recorded at the Wuhan station. There is still a westerly jet stream with wind speed greater than
 433 20m/s beyond the upper-air of 500hPa level. The east of Wuhan proximity to the main body of convection, the
 434 reduction in energy suggests intensive of upward motion, leading to the reduction of effective potential energy
 435 and further develop of convective. Notably, the GTS12 radiosonde, launched from Wuhan, ceased data
 436 collection after the ascent phase, thus missing this crucial change. The descent phase of ADDR5 demonstrates
 437 robust monitoring capabilities and holds significant implications, as it can timely captures environmental
 438 conditions favorable for convection onset and development, including wind patterns, effective potential energy,
 439 and humidity at downstream locations. These findings enable researchers to analyze changes in the upper-air
 440 field and the occurrence of catastrophic weather convective systems.



441

442 **Figure 9. Comparison of ADDRS and GTS12 radiosonde T-logP at the Wuhan station: (a) GTS12 radiosonde; (b)**
 443 **ascent phase of ADDRS radiosonde; (c) descent phase of ADDRS radiosonde.**

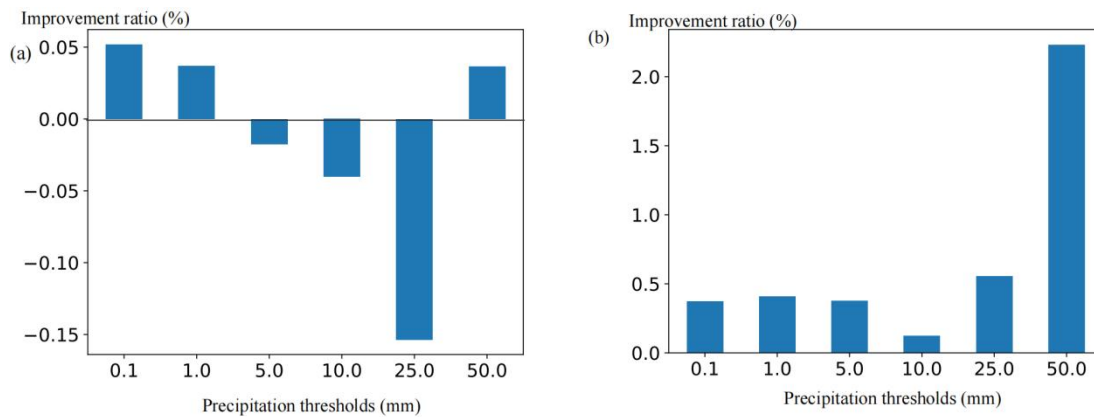
444 **5.2 Applications in numerical weather prediction (NWP)**

445 Compared with GTS12 radiosondes, the ADDRS radiosondes of ascent and descent phase measurement
 446 data for numerical weather prediction (NWP), achieving a similar role to intensive sounding and providing more
 447 continuous, direct stratospheric measurement data (Zhang, X et al., 2025; Zhang, X.P et al. 2023). The
 448 Numerical Department of the China Meteorological Administration developed the key technology for ADDRS
 449 assimilation in the CMA-MESO 3DVar (three-dimensional variational mesoscale) (Zhuang et al. 2019) and
 450 CMA-GFS 4DVar systems (four-dimensional Variational Global Forecast System) (Wang, R. W et al., 2021).
 451 To avoid the tangent linear and adjoint models, the four-dimensional ensemble forecast error is introduced into
 452 the CMA global data assimilation system, and the Hybrid-4DVar assimilation scheme is developed. The
 453 batch cycling forecast experiments and typhoon forecast experiments are conducted and compared with the
 454 4DVar scheme (Gong et al., 2019; Wang, F et al., 2024). Specifically, this includes observation operators that
 455 consider drift positions and vertical spacing methods, such as selecting the nearest radiosonde data from the
 456 model layer for assimilation. We employed the CMA-MESO system to conduct a measurement data
 457 assimilation in the ADDRS descent phase across six test stations in the middle and lower reaches of the Yangtze
 458 River from July 1 to July 31, 2021. We set up the control test (CTL) as in the CMA-MESO system, and the
 459 observed data included traditional sounding data, ground reports, aircraft reports, cloud-guided wind, radar
 460 radial wind, GNSS occultation refractive index, and ground-based GNSS retrieval of the atmospheric whole-
 461 layer precipitation water. ADDRS data assimilation was added to the control CTL in the Down test.

462 The impact of the ADDRS descent phase measurement data on the precipitation forecast at CMA-MESO at
 463 03, 06, 09, 15, 18, and 21 UTC (termed the warm start times) was evaluated. Compared to the TS (Threat Score),
 464 the ETS (Equitable Threat Score) imposes stricter penalty for false alarms and missed reports, making the
 465 scoring more equitable. The results of the one-month batch test indicate that assimilating ADDRS descent phase
 466 data improves precipitation forecasting skills, especially for heavy precipitation above a certain magnitude. Fig.
 467 10a and Fig. 10b illustrate the improvement rates in accumulated precipitation forecasting skills for the 0-12
 468 hour and 12-24 hour periods from the warm start time. Positive values indicate that the precipitation forecasting
 469 skills of the Down test are improved compared with those of the CTL test, while negative values indicate a
 470 decrease in forecasting skills for the Down test. The ETS scores for precipitation forecasts in the 0-12 hour
 471 range at thresholds of 0.1 mm, 1 mm, and 50 mm increased slightly, averaging about 0.04% (Fig. 10a). Due to

472 the timeliness required for forecasting, the 12-24 hour precipitation forecast is of particular interest to
 473 forecasters. As illustrated in Fig. 10b, the Down test demonstrated enhanced ETS scores for precipitation
 474 forecasts across all levels within the 12-24 hour range, with an average increase of 0.7% at the 50 mm
 475 threshold and a notable 2.2% improvement specifically at this level. It is important to note that while these ETS
 476 improvements are consistent and positive, they have not yet reached conventional levels of statistical
 477 significance (e.g., $p < 0.05$) over the one-month test period, primarily due to the limited sample size of case
 478 studies. This underscores the preliminary yet promising nature of these findings.

479 In addition, we utilized CMA-MESO V5.1 to conduct Observing System Simulation Experiments (OSSE)
 480 under the ADDRS network nationwide. The results indicate that once the ADDRS network observation is
 481 implemented, the national precipitation forecast skills of the CMA-MESO fast cycle assimilation forecast
 482 system at warm startup time can improve by 2%-5%. The potential operational applications of ADDRS high-
 483 resolution data were quantitatively evaluated using a numerical model (Wang, R. W et al., 2023). After the
 484 application of ADDRS data in CMA-GFS 4DVar assimilation, the temperature analysis error at 06:00 and 18:00
 485 was reduced by more than 2% and the average prediction skill of the CMA-MESO accumulated precipitation
 486 results for the 12-36 hour period improved by 1% (Wang, J. C. et al., 2024).



487
 488 **Figure 10. Improvement rates of cumulative precipitation thresholds (mm) predictions for 0-12 hours (a) and 12-24**
 489 **hours (b) in the Down test compared to the control test.**

490 5.3 Applications in targeted observations

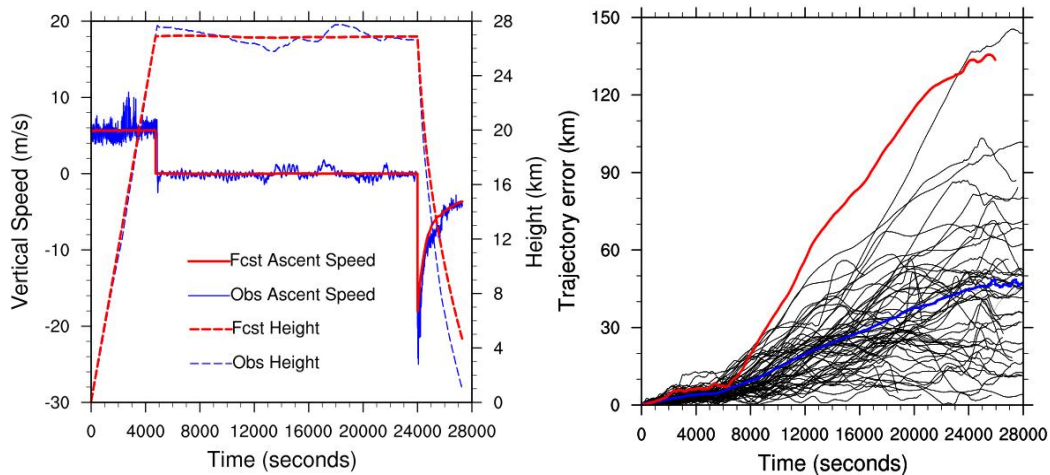
491 Targeted observation have sometimes been one of frontier field in atmospheric science research. They
 492 represent a possible method to address the shortcomings of operational observation systems in monitoring
 493 extreme weather events. Furthermore, they sometimes enhance the initial field quality and forecast accuracy of
 494 numerical models (Majumdar., 2016). With its capacity for “ADD” measurement, the ADDRS has the potential
 495 to conduct targeted observations in uninhabited areas, rarely observed regions, and during specific extreme
 496 weather events. However, since the ADDRS lacks a steering system, accurate trajectory prediction is essential
 497 for utilizing the descent phase for vertical measurements in these locations. This requires careful consideration
 498 of appropriate drift height, launch time, and launch location, allowing the ADDRS sounding to be carried to the
 499 target observation area by the ambient wind field.

500 In this context, a trajectory prediction and selection method based on high-resolution numerical weather
 501 prediction technology has been proposed for ADDRS (Wang, J. C et al., 2021). Additionally, Majumdar (2016)

502 highlights that advancements in numerical weather prediction (NWP) systems—such as improved data
 503 assimilation techniques and enhanced model resolution—have reduced the marginal contributions of individual
 504 observing systems. Furthermore, the evaluation of targeted observations is constrained by factors including
 505 flow-dependent conditions, limited sample sizes, and inconsistencies in verification metrics. Therefore, cost-
 506 effective strategies for targeted observations necessitate exploration through multi-agency coordinated
 507 observing system experiments, such as FSO studies (Magnusson.et al., 2025).

508 5.3.1 Trajectory prediction method and software system

509 The issues of low temporal resolution and prediction accuracy associated with the linear extrapolation
 510 method used in balloon trajectory prediction (Brown et al., 2024). The balloon trajectory equation is directly
 511 embedded into a high-resolution numerical weather model system that utilizes a model atmospheric
 512 environment with high temporal resolution (1-10 seconds) and high spatial resolution (1-3 km). This approach
 513 enables precise simulation of vertical velocity during the ADDRS descent phase (Fig. 11a), enhancing the
 514 accuracy of ADDRS trajectory prediction and the simulation of descent velocity. The average prediction error
 515 for a 6-hour trajectory is less than 40 km (Fig. 11b).



516

517 **Figure 11. (a) Comparison of simulated (red line) and observed (blue line) vertical speeds of ADDRS radiosonde data**
 518 **during the descent phase at the Anqing station at 11:17 on June 20, 2018; (b) Deviations of 63 pairs of simulated**
 519 **ADDRS trajectories versus observed trajectories (black line), with the average deviation indicated by the blue line**
 520 **and the largest forecast deviation shown by the red line.**

521 5.3.2 Trajectory selection method based on the collection idea

522 To observe the ADDRS in the target observation area, we proposed a method of elevation selection based
 523 on ensemble forecasting, considering the characteristics of the atmospheric wind field as it varies with altitude.
 524 The main idea of this method is to predict the trajectories of all ADDRS stations at different drifting heights and
 525 select the heights closest to the target observation area. The details are as follows:

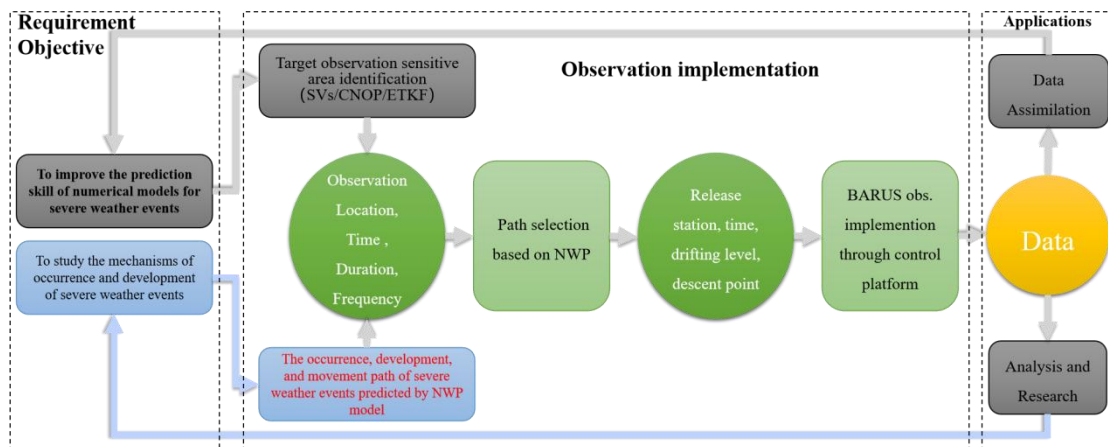
- 526 1. Identify the positions and launch time: Given the positions $S_m(x_m, y_m, z_m)$ of M ADDRS launch stations and
 527 the launch time t_r .
- 528 2. Select safe drift heights: Choose N safe drift heights h_1, h_2, \dots, h_n , that comply with civil aviation safety
 529 regulations as flat drift heights.

- 530 3. Trajectory prediction: Utilize the trajectory prediction system to predict the ADDRS trajectories under the
 531 above conditions within 12 hours, resulting in $T_{nm}(x,y,z,t)$ for N trajectories at each of the M launch
 532 stations.
- 533 4. Calculate closest trajectory: From the $M \times N$ trajectories obtained in step 3, calculate the trajectory closest
 534 to the target observation point. When the distance is less than the predetermined standard distance L_C that
 535 can meet the requirements, the releasing ADDRS station and the drifting height H_s are selected, and the
 536 time nearest to the target area is taken as the descent time t_s . If no suitable drift height meets the conditions,
 537 the trajectory selection fails.
- 538 5. Implement target observation: Input the information regarding the ADDRS balloon launch station, drift
 539 height, and descent time determined in step 4 into the ADDRS operation command system to execute the
 540 target observation.

541 **5.3.3 Targeted observations experiment of Typhoon**

542 The ADDRS research team proposed a 'full chain' implementation for target observation using ADDRS
 543 (Fig. 12). This implementation plan, designed to provide technical support for ADDRS applications in disaster
 544 weather monitoring, forecasting, and mechanism research, encompasses three primary phases. Initially, the
 545 requirements for target observation are established. These requirements fall into two categories: one focusing on
 546 specific disaster weather events and the other on sensitive areas to improve future numerical prediction skills.
 547 The target observation area is then determined based on the type of demand. For the first category, the specific
 548 location of anticipated disaster weather is identified through numerical prediction results. For the second
 549 category, the target observation location is determined using CMA-GFS singular vector technology.

550 Subsequently, the trajectory selection system is invoked to ascertain the ADDRS discharge radiosonde
 551 observations station, drift height, discharge time, and other relevant information. This information is then
 552 transmitted to the operation command system of ADDRS to guide the stations in implementing ADDRS
 553 measurements. Ultimately, the ADDRS target observation data is distributed to users for application and
 554 evaluation.

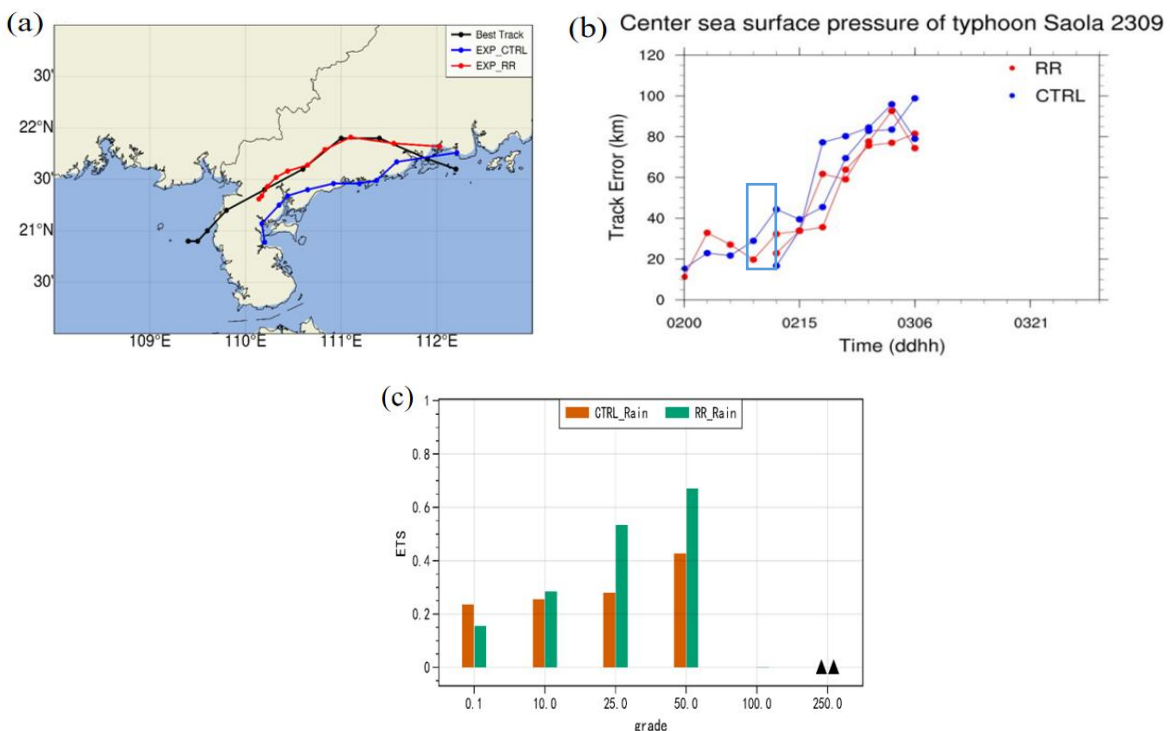


555
 556 **Figure 12. Technical route for targeted observations of typhoons and other severe weather using ADDRS and CMA-**
 557 **MESO models.**

558 According to the implementation plan for ADDRS target observation (Zhang et al., 2021; Liu, L. H et al.,
 559 2022), we made a preliminary attempt to conduct a target observation experiment on Typhoon 2309 'SAOLA'

560 (Lau et al., 2024) formed at 00 UTC on August 28, 2023. By 00 UTC on September 1, it was expected that
 561 'SAOLA' would land near Guangdong on September 2nd. Therefore forecasters sought profiles of the inner
 562 structure of Typhoon 'SAOLA'. Note also the importance of the steering flow and use of satellite data to analyse
 563 the wider environment of tropical storms (Magnusson et al, 2025). Using the typhoon trajectory predicted by
 564 CMA-GFS, we pinpointed the typhoon's position for 12:00 PM on September 2 post-landfall. The ADDRS
 565 trajectory selection system was then engaged to ascertain the balloon launch station and drift height that could
 566 reach or come closest to the typhoon area, ranging from the minimum navigation safety height of 21 km to 29
 567 km. We set ten different drift levels at 1 km intervals, with trajectory predictions and simulations conducted
 568 from four radiosonde observations stations in Guangdong. Yangjiang radiosonde observations station in
 569 Guangdong was ultimately chosen for the launch, scheduled for 06:00 on September 2, 2023, with a drift level
 570 of 25 km.

571 We calculated the required hydrogen capacity for the dual-mode balloon, and the 'ADD' subsystem was
 572 prepared to be deployed by radiosonde observations station personnel. When the radiosonde reached the core
 573 area of 'SAOLA' the radiosonde dispatched commands to the 'SAOLA' controller via control command
 574 transmission equipment, successfully observing the descent phase 80 km from the center of Typhoon 'SAOLA'
 575 The obtained ADDRS data was subsequently assimilated into the CMA_MESO 3DVar system. Test results
 576 indicated that after assimilating the data from the ADDRS descent phase, the forecast error for the typhoon
 577 trajectory reported since 06:00 on September 2, 2023, was reduced. Specifically, the typhoon trajectory error at
 578 02:18 was reduced from 62.7 km to 35 km in the control test ,marking an improvement of 44.18%. Additionally,
 579 precipitation forecasting techniques exhibited improvements: from 0.25 to 0.30 in the 10 mm scale, from 0.30 to
 580 0.55 in the 25 mm scale, and from 0.45 to 0.70 in the 50 mm scale. These results effectively demonstrate the
 581 potential of ADDRS in target observation and numerical assimilation applications (Fig. 13). It is worth noting
 582 that the initial use of ADDRS for target observation served as a foundational attempt, paving the way for future
 583 ADDRS operations and maximizing its utility (Wen., et al., 2024).



584

585

586 **Figure 13. 2023-09-02 UTC 00-12h: (a) Control test (blue), ADDRS data assimilation impact test (red), and optimal**
587 **trajectory of Typhoon 'Saola' (black); (b) Comparison of sea level pressure at the central point of Typhoon 'Saola'**
588 **between the control test (blue) and the ADDRS data assimilation impact test (red); (c) ETS scores for 0-24 hours of**
589 **precipitation forecast from control trials (orange) and ADDRS data assimilation impact trials (green).**

590 **6. Summary**

591 ADDRS represents a possible next-generation approach, surpassing the 20th century operational method.
592 We developed a multi-station real-time reception system utilizing 'Internet cloud + Instruments terminal'
593 technology. Additionally, uplink commands can be sent from the ground to facilitate descent measurements in
594 designated areas and targeted observations in weather-sensitive regions. Following over five years of extensive
595 research and numerous field tests, the instruments, software, and operational guidelines of the system have
596 achieved a refined level of maturity. Starting January 1, 2024, ADDRS already undergo operational experiments
597 at four radiosonde observations stations in Guangdong, China. Since July 2024, a planned operational trial at
598 127 CMA radiosonde observations stations aims to achieve full operational capability across all CMA
599 radiosonde observations stations by 2026. The positive impact of ADDRS data assimilation demonstrated here,
600 even if not yet statistically significant over a one-month sample, has shown considerable operational promise.
601 We are confident that statistically significant improvements in precipitation forecast skills will be achieved as
602 the data records lengthen and the number of case studies, particularly for extreme precipitation events, increases
603 in the future. ADDRS is a situational profiling technique that offers cost-effective upper-air measurements,
604 making it suitable for widespread application in operational soundings. However, challenges remain, such as
605 improving the drift success rate, enhancing relevant technologies, and fully leveraging the potential of
606 continuous measurement data during the drift phase. With the constant development of ADDRS and the
607 continuous deepening of the measurement data, ADDRS will become a development direction for future
608 operational upper-air observation applications and scientific research.

609
610 **Acknowledgments:** The authors are thankful to the Editor and all anonymous reviewers for their help in im-
611 proving this manuscript.

612 **Data Availability Statement:** The ADDRS research team is currently building a new data-sharing
613 platform(<https://www.r7tec.com/html/report/20040875-1.htm>), which will be available for scientific sharing to
614 registered users starting in December this year. More data acquisition requires formal request to the
615 corresponding author <gqyaoc@cma.gov.cn> for restricted availability.

616 Xiaozhong Cao*1, Qiyun Guo2, Haowen Luo2, Rongkang Yang2, Guo Jianping3, Jincheng Wang4, Die
617 Xiao5, Jianping Du6, Zhongliang Sun7, Shijun Liu8, Sijie Chen9, Anfan Huang2, Peng Zhang*2

618
619 Author contributions. XC, PZ, QG and HL designed the experiments and wrote the paper; JW, DX, JD, ZS, SL
620 carried out the experiments; RY, JW analyzed the experimental results. GJ, SC, AH revised the paper and
621 participated in the discussion.

622 Competing interests. The contact author has declared that none of the authors has any competing interests.

623 Disclaimer. Publisher's note: Copernicus Publications remains neutral with regard to jurisdictional claims made
624 in the text, published maps, institutional affiliations, or any other geographical representation in this paper.

625 While Copernicus Publications makes every effort to include appropriate place names, the final responsibility
626 lies with the authors.

627 Financial support. This research has been supported by the National Natural Science Foundation of China (grant
628 no. U2442214) ; the National Key Research and Development Program (grant no. 2018YFC1506200) ;the
629 Innovation Team of the China Meteorological Administration(grant no. CMA2023QN11)..

630

631 **REFERENCES**

- 632 Anand, D., Kumar, B. S., and Ojha, D.: TIFR Zero-Pressure balloon program crosses a milestone, *Current*
 633 *Science*, 2021, 120, 1672-1678, doi:<https://doi.org/10.18520/cs/v120/i11/1672-1678>.
- 634 Bauer, P., Thorpe, A., Brunet, G.: The quiet revolution of numerical weather prediction, *Nature*, 2015, 525, 47–
 635 55, doi:<https://doi.org/10.1038/nature14956>.
- 636 Bormann, N., Lawrence, H., Farnan, J.: Global observing system experiments in the ECMWF assimilation
 637 system, *ECMWF Technical Memorandum*, 2019, 839, 24 pp., doi:<https://doi.org/10.21957/sr184iyz>.
- 638 Bauer, P., G. Radnóti., S. Healy., C. Cardinali.: GNSS Radio Occultation Constellation Observing System
 639 Experiments, *Mon. Wea. Rev.*, 2014, 142, 555–572, doi:<https://doi.org/10.1175/MWR-D-13-00130.1>
- 640 Brown, D., Linz, M. & Leidich, J. Seasonal and geographic viability of high altitude balloon navigation. *Sci*
 641 *Rep* 14, 21861 (2024). doi:<https://doi.org/10.1038/s41598-024-71445-9>.
- 642 Cohn, S. A., and Coauthors, 2013: Driftsondes: Providing In Situ Long-Duration Dropsonde Observations over
 643 Remote Regions. *Bull. Amer. Meteor. Soc.*, 94, 1661–1674, doi:[https://doi.org/10.1175/BAMS-D-12-](https://doi.org/10.1175/BAMS-D-12-00075.1)
 644 [00075.1](https://doi.org/10.1175/BAMS-D-12-00075.1).
- 645 Cao, X. Z., Xia, Y. C., Luo, H. W., Liu, L. H., Liu, Y. F., Liu, Z. Y., Li, X., Guo, R., and Guo, Q. Y.: Technical
 646 development and prospect of meteorological sounding measurement, *J. Adv. Meteorol. Sci. Technol*, 12,
 647 27-36, 2022, doi:<https://doi.org/10.3969/j.issn.2095-1973.2022.05.005>.(in Chinese)
- 648 Cao, X. Z., Guo, Q. Y., Yang, R. K.: Research of rising and falling twice sounding based on long-time interval
 649 of flat-floating, *Chinese Journal of Scientific Instrument*, 2019,40(2): 198-204.
 650 <http://yqyb.etmchina.com/yqyb/article/abstract/20190223?st=search>. (in Chinese)
- 651 DuBois, J. L., Multhaupt, R. P., and Ziegler, C. A.: Invention and Development of the Radiosonde with a Catalog
 652 of Upper-Atmospheric Telemetering Probes in the National Museum of American History, Smithsonian
 653 Institution, *Smithsonian Studies in History and Technology*, 2002, 53, 1-78,
 654 doi:<https://doi.org/10.5479/si.00810258.53.1>.
- 655 Fujiwara, M., Sun, B., Reale, A., Cimini, D., Larosa, S., Borg, L., von Rohden, C., Sommer, M., Dirksen, R.,
 656 Maturilli, M., Vömel, H., Kivi, R., Ingleby, B., Kramer, R. J., Demoz, B., Madonna, F., Carminati, F.,
 657 Lewis, O., Candy, B., Thomas, C., Edwards, D., Noersomadi, Shimizu, K., and Thorne, P.: Justification for
 658 high-ascent attainment for balloon radiosonde observations at GRUAN and other sites, *Atmos. Meas.*
 659 *Tech.*, 2025, 18, 2919–2955, doi:<https://doi.org/10.5194/amt-18-2919-2025>.
- 660 Gallice, A., Wienhold, F. G., Hoyle, C. R., Immler, F., and Peter, T.: Modeling the ascent of sounding balloons:
 661 derivation of the vertical air motion, *Atmos. Meas. Tech.*, 2011, 4, 2235-2253,
 662 doi:<https://doi.org/10.5194/amt-4-2235-2011>.
- 663 Gong, N., Liu, Y. F., Ren, J., Wu, Q., and Hu, H. L.: A Novel Adaptive Resource Allocation Framework for
 664 Sounding Networks, 2021 the 11th International Workshop on Computer Science and Engineering (WCSE
 665 2021) 276-283, doi:<https://doi.org/10.18178/wcse.2021.06.040>.
- 666 Guo, Q. Y., Yang, J. C., Yang, R. K., Qian, Y., and Cao, X. Z.: Evaluation of wind performance of domestic
 667 Beidou dropsonde of ball-loading, *J. Nanjing Univ. Inf. Eng.: Nat. Sci. Ed.*, 10,
 668 12, doi:<https://doi.org/10.13878/j.cnki.jnuist.2018.05.014>, 2018.(in Chinese)

669 Gong, J. D., Liu, Y. Z., Zhang, L.: A study of simplification and linearization of the NSAS deep convection
670 cumulus parameterization scheme for 4D-Var, *Acta Meteorologica Sinica*, 2019, 77, 595-616,
671 doi:<https://doi.org/10.11676/qxxb2019.048>.(in Chinese)

672 Haig, T. O., and V. E. Lally, 1958: Meteorological Sounding Systems. *Bull. Amer. Meteor. Soc.*, 39, 401–
673 409, doi:<https://doi.org/10.1175/1520-0477-39.8.401>.

674 He, Y., Zhu, X., Sheng, Z., and He, M.: Identification of stratospheric disturbance information in China based
675 on the round-trip intelligent sounding system, *Atmos. Chem. Phys.*, 2024, 24, 3839–3856,
676 doi:<https://doi.org/10.5194/acp-24-3839-2024>.

677 Hersbach, H., Bell, B., Berrisford, P., Hirahara, S., Horányi, A., Muñoz - Sabater, J., Nicolas, J., Peubey, C.,
678 Radu, R., Schepers, D., Simmons, A., Soci, C., Abdalla, S., Abellan, X., Balsamo, G., Bechtold, P., Biavati,
679 G., Bidlot, J., Bonavita, M., De Chiara, G., Dahlgren, P., Dee, D., Diamantakis, M., Dragani, R., Flemming,
680 J., Forbes, R., Fuentes, M., Geer, A., Haimberger, L., Healy, S., Hogan, R. J., Hólm, É., Janisková, M.,
681 Keeley, S., Laloyaux, P., Lopez, P., Lupu, C., Radnoti, G., de Rosnay, P., Rozum, I., Vamborg, F.,
682 Villaume, S., Thépaut, J. - N.: The ERA5 global reanalysis, *Q. J. R. Meteorolog.*
683 *Soc.*, doi:<https://doi.org/10.1002/qj.3803>, 2020.

684 Ingleby, B., and Coauthors, 2016: Progress toward High-Resolution, Real-Time Radiosonde Reports. *Bull.*
685 *Amer. Meteor. Soc.*, 97, 2149–2161, doi:<https://doi.org/10.1175/BAMS-D-15-00169.1>.

686 Ingleby, B., Rodwell, M., Isaksen, L.: Global radiosonde network under pressure, *ECMWF Newsletter No. 149*
687 – Autumn 2016, pp. 25 - 30, doi:<https://www.ecmwf.int/sites/default/files/elibrary/2016/18147-global-radiosonde-network-under-pressure.pdf>.

689 Ingleby, B., 2021: Use of radiosonde descent data from ships, *ECMWF Newsletter*, Page 5
690 doi:[https://www.ecmwf.int/sites/default/files/elibrary/102021/20225-newsletter-no-169-autumn-](https://www.ecmwf.int/sites/default/files/elibrary/102021/20225-newsletter-no-169-autumn-2021_1.pdf)
691 [2021_1.pdf](https://www.ecmwf.int/sites/default/files/elibrary/102021/20225-newsletter-no-169-autumn-2021_1.pdf).

692 Ingleby, B., Motl, M., Marlton, G., Edwards, D., Sommer, M., von Rohden, C., Vömel, H., and Jauhiainen, H.:
693 On the quality of RS41 radiosonde descent data, *Atmos. Meas. Tech.*, 2022, 15, 165-
694 183, doi:<https://doi.org/10.5194/amt-15-165-2022>.

695 Johnson, A., Wang, X., Hutchinson, T., and Creus-Costa, J.: Impact of WindBorne observation assimilation on
696 prediction of a TPV merger case from THINICE, *J. Geophys. Res. Atmospheres*, 2024, 129,
697 e2024JD041395, doi:<https://doi.org/10.1029/2024JD041395>.

698 Jensen, M. P., Holdridge, D. J., Survo, P., Lehtinen, R., Baxter, S., Toto, T., and Johnson, K. L.: Comparison of
699 Vaisala radiosondes RS41 and RS92 at the ARM Southern Great Plains site, *Atmos. Meas. Tech.*, 2016, 9,
700 3115–3129, doi:<https://doi.org/10.5194/amt-9-3115-2016>.

701 Liu, S. J., Yang, R. K., Cao, X. Z., Guo, Q. Y., Cheng, K. Q., Kan, Z. P., and Wang, J. C.: Analysis and
702 Numerical Experiment of the Horizontal Drift Round-trip Sounding Balloon's Dynamic and Thermal
703 Process in the Adjacent Space, *Chin. J. Atmos. Sci.*, 2022, 46, 788–
704 804, doi:<https://doi.org/10.3878/j.issn.1006-9895.2110.20252>.(in Chinese)

705 Liu, Y. F., Zhou, Y. Y., Du, J. P., Liu, D., Ren, J., Chen, Y. H., Zhang, F., and Chen, J. P.: RTP-GRU:
706 Radiosonde Trajectory Prediction Model Based on GRU, in *Proceedings.*, 2021, 24, 10.1007/978-981-15-
707 8462-6_61.

708 Liu, B., Guo, J., Gong, W., Zhang, Y., Shi, L., Ma, Y., Li, J., Guo, X., Stoffelen, A., de Leeuw, G., and Xu, X.:
709 Intercomparison of wind observations from ESA's satellite mission Aeolus, ERA5 reanalysis and
710 radiosonde over China, *Atmos. Chem. Phys. Discuss.* [preprint], <https://doi.org/10.5194/acp-2021-41>, 2021.

711 Liu, L. H.; Han, Y.; Xia, Y. C.; Guo, Q. Y.; Gao, W.; Guo, J. P.: Investigation of Atmospheric Dynamic and
712 Thermodynamic Structures of Typhoon Sinlaku (2020) from High-Resolution Dropsonde and Two-Way
713 Rawinsonde Measurements. *Remote Sens.* 2022, 14, 2704. doi:<https://doi.org/10.3390/rs14112704>.

714 Lau, D.S., Chan, W.S., Wong, Y.C., Lam, C.C., Chan, P.W.: Hindcast Insights from Storm Surge Forecasting of
715 Super Typhoon Saola (2309) in Hong Kong with the Sea, Lake and Overland Surges from Hurricanes
716 Model, *Atmos.*, 2024, 15, 17, doi:<https://doi.org/10.3390/atmos15010017>.

717 Newman, S., Carminati, F., Lawrence, H., et al. Assessment of new satellite missions within the framework of
718 numerical weather prediction, *Remote Sensing*, 2020,12(10), 1580, doi:10.3390/rs12101580.

719 Majumdar, S.J.: A review of targeted observations, *Bull. Am. Meteorol. Soc.*, 2016, 97, 2287-
720 2303, doi:<https://doi.org/10.1175/BAMS-D-14-00259.1>.

721 Magnusson, L., Majumdar, S.J., Dahoui, M.L., Bormann, N., Bonavita, M., Browne, P.A., Brown, A.R., De
722 Chiara, G., Duncan, D.I., English, S., Geer, A.J., Healy, S., Ingleby, B., McNally, A.P., Pappenberger, F.,
723 Prates, F., Rabier, F., de Rosnay, P., Rennie, M.P., Warrick, F.: The role of observations in ECMWF
724 tropical cyclone initialisation and forecasting, *Q. J. R. Meteorolog. Soc.*, 2025, 151(768),
725 e4924, doi:<https://doi.org/10.1002/qj.4924>.

726 Pettifer, R. E.: From Observations to Forecasts - Part 2. The development of in situ upper air measurements,
727 *Weather*, 2009, 64, doi:<https://doi.org/10.1002/wea.484>.

728 Raman, M. R., Ratnam, M. V., Rajeevan, M., Rao, V. V. M. J., Rao, S. V. B.: Intriguing Aspects of the
729 Monsoon Low-Level Jet over Peninsular India Revealed by High-Resolution GPS Radiosonde
730 measurements, *J. Atmos. Sci.*, 2011, 68, 1413–1423, doi:<https://doi.org/10.1175/2011JAS3611.1>.

731 Roth, S., & Yoder, C. D.: Balloon missions soar to new heights. *Aerospace America*, 2022, 60(11), 35-35.
732 doi:<https://aerospaceamerica.aiaa.org/year-in-review/balloon-missions-soar-to-new-heights>.

733 Ratnam, M. V., Pravallika, N., Babu, S. R., Basha, G., Pramitha, M., Murthy, B. V. K.: Assessment of GPS
734 radiosonde descent data, *Atmos. Meas. Tech.*, 2014, 7(4), doi:<https://doi.org/10.5194/amt-7-1011-2014>.

735 Seidel, D. J., Berger, F. H., Diamond, H. J., Dykema, J., Goodrich, D., Immler, F., Murray, W., Peterson, T.,
736 Sisterson, D., Sommer, M., Thorne, P., Vomel, H., & Wang, J.: Reference Upper-Air Observations for
737 Climate: Rationale, Progress, and Plans. *Bulletin of the American Meteorological Society*, 2009, 90(3),
738 361-369. doi:<https://doi.org/10.1175/2008BAMS2540.1>

739 Shen, Z. P., Pan, X. Z., and Yi, Y. L.: Preparation and properties of modified nano-clay/natural latex composites,
740 *J. Rubber Ind.*, 2020, 67, 4, doi:<https://doi.org/10.12136/j.issn.1000-890X.2020.08.0580>.(in Chinese)

741 Tan, X. W., Chen, D. H., Zhang, Q. H.: An impact study of a new type of data of adaptive or targeting
742 observation on typhoon forecast, *J. Trop. Meteorol.*, 2006, 22(1), 18–
743 25, doi:<https://doi.org/10.3969/j.issn.1004-4965.2006.01.003>.(in Chinese)

744 Vernier, J. - P., Fairlie, T. D., Deshler, T., Ratnam, M. V., Gadhavi, H., Kumar, B. S., Natarajan, M., Pandit, A.
745 K., Raj, S. T. A., Kumar, A. H., Jayaraman, A., Singh, A. K., Rastogi, N., Sinha, P. R., Kumar, S., Tiwari,
746 S., Wegner, T., Baker, N., Vignelles, D., Stenchikov, G., Shevchenko, I., Smith, J., Bedka, K., Kesarkar, A.,
747 Singh, V., Bhate, J., Ravikiran, V., Rao, M. D., Ravindrababu, S., Patel, A., Vernier, H., Wienhold, F. G.,

748 Liu, H., Knepp, T. N., Thomason, L., Crawford, J., Ziemba, L., Moore, J., Crumeyrolle, S., Williamson,
749 M., Berthet, G., Jégou, F., Renard, J. B.: BATAL: The Balloon Measurement Campaigns of the Asian
750 Tropopause Aerosol Layer, *Bull. Am. Meteorol. Soc.*, 2018, 99, 955–
751 973, doi:<https://doi.org/10.1175/BAMS-D-17-0014.1>.

752 Vernier, H., Rastogi, N., Liu, H., Pandit, A. K., Bedka, K., Patel, A., Ratnam, M. V., Kumar, B. S., Zhang, B.,
753 Gadhavi, H., Wienhold, F., Berthet, G., and Vernier, J.-P.: Exploring the inorganic composition of the
754 Asian Tropopause Aerosol Layer using medium-duration balloon flights, *Atmos. Chem. Phys.*, 2022, 22,
755 12675–12694, doi:<https://doi.org/10.5194/acp-22-12675-2022>.

756 WMO (World Meteorological Organization): 8th WMO Workshop on the Impact of Various Observing Systems
757 on Numerical Weather Prediction and Earth System Prediction, Norrköping, Sweden, 27 - 30 May 2024,
758 doi:<https://community.wmo.int/en/meetings/8th-wmo-impact-workshop-home>.

759 Wang, J. H. , Young, K., Hock, T., Lauritsen, D., Behringer, D., Black, M., Black, P. G., Franklin, J., Halverson,
760 J., Molinari, J., Nguyen, L., Reale, T., Smith, J., Sun, B., Wang, Q., Zhang, J. A.: A long-term, high-quality,
761 high-vertical resolution GPS dropsonde data set for hurricane and other studies, *Bull. Am. Meteorol. Soc.* ,
762 2015, 96, 961-973, doi:<https://doi.org/10.1175/BAMS-D-13-00203.1>.

763 WMO (World Meteorological Organization): Guide to Meteorological Instruments and Methods of Observation,
764 Volume III - Observing Systems, WMO-No. 8, 2025 edition, Page 464, pp.,
765 doi:<https://library.wmo.int/idurl/4/41650>.

766 WMO (World Meteorological Organization): Instruments and Observing Methods Report No. 143: Report of
767 WMO's 2022 Upper-Air Instruments Intercomparison Campaign, Geneva, 2024, 22
768 pp., doi:<https://library.wmo.int/idurl/4/68808>.

769 WMO (World Meteorological Organization): The gaps in the Global Basic Observing Network (GBON), SOFF
770 Series No. 2, 2020, Page 4, pp., doi:<https://library.wmo.int/idurl/4/57174>.

771 Wang, D., Wang, J. C., Tian, W. H., Guo, Q. Y.: Quality control and uncertainty analysis of Round - trip
772 drifting sounding system data, *Chinese J. Atmos. Sci.*, 2020, 44,
773 20, doi:<https://doi.org/10.3878/j.issn.1006-9895.1912.19203>. (in Chinese)

774 Wang, R. W., Han, W., Tian, W. H., Gong, J. D.: Blacklist Design of AMDAR Temperature Data and Their
775 Application in the CMA-GFS, *J. Trop. Meteorol.*, 2021, 27, 368–377, doi:<https://doi.org/10.46267/j.1006-8775.2021.032>.

776

777 Wang, F., Gong, J. D., Wang, R. C., Chen, Y. D.: A methodological study of the CMA global hybrid four-
778 dimensional variational data assimilation system, *Acta Meteorol. Sin.*, 2024, 82(5), 709–
779 720, doi:<https://qxxb.cmsjournal.net/cn/article/doi/10.11676/qxxb2024.20230140>. (in Chinese)

780 Wang, R. W., Wang, J. C., Wang, D., Tao, Y. W., Tian, W. H.: Study on the Influence of Return Sounding
781 Observation System Based on CMA-MESO, *Meteorol. Mon.*, 2023, 49(1), 52–
782 61, doi:<https://doi.org/10.7519/j.issn.1000-0526.2022.032601>. (in Chinese)

783 Wang, J. C., Wang, D., Wang, R. W., Tan, J., Rong, N.: Assimilation of Round-Trip Horizontal Drift
784 Radiosonde Data in CMA-MESO 3DVar and Its Impact on Model Forecast, *Meteorol. Mon.*, 2024, 50(2),
785 50–60, doi:<https://doi.org/10.7519/j.issn.1000-0526.2023.110501>. (in Chinese)

786 Wang, J. C., Wang, D., Yang, R. K., Cao, X. Z., Guo, Q. Y.: A Return Radiosonde Trajectory Forecast Method
787 and Its Preliminary Evaluation Based on High Resolution Numerical Weather Prediction Model, Chinese J.
788 Atmos Sci., 2021, 45, 651–663, doi:<https://doi.org/10.3878/j.issn.1006-9895.2012.20186>.

789 Wen, Q. S., Zhang, X. F., Hu, S., Zhao, P. T., Zhong, S. X., Liu, Z. Y., Zhao, Z. K., Liang, J. H., Dai, G. F.,
790 Zhang, C. Z., Li, M. J., Huang, L.: Collaborative assimilation experiment of Beidou radiosonde and drone-
791 dropped radiosonde based on CMA-TRAMS, Atmos. Oceanic Sci. Lett., 2025,
792 18(2), doi:<https://doi.org/10.1016/j.aosl.2024.100555>.

793 Xu, H. F., Guo, Q. Y., Liu, Y. Z., et al.: Key factors influencing drift success rate of new-type meteorological
794 balloons, Journal of Applied Meteorological Science, 2025, 36(4), 427-440.
795 doi:<https://doi.org/10.11898/1001-7313.20250404>.(in Chinese)

796 Yang, R. K., Wang, Y., and Liu, Q. Q.: Dynamic Performance Analysis of Sounding temperature sensor, Sci.
797 Technol. Eng., 2014, doi:<https://doi.org/10.3969/j.issn.1671-1815.2014.04.012>.(in Chinese)

798 Yang, J. C., et al: Research on error prediction technology of radiosonde temperature sensor, Journal of
799 Electronic Measurement and Instrumentation, 2022, 35(12):24-26.
800 doi:<https://doi.org/10.13382/j.jemi.B2104288>.(in Chinese)

801 Yao, L.B., Shen, D., Sun, X., Wang, D.H., Cao, X.Z., Wang, J.C., Wang, D., Zhang, C.Y., Guo, Q.Y., 2026.
802 Ascent-drift-descent radiosonde system: Field experiments and data quality assessment. Atmospheric
803 Research. 329, 108489. <https://doi.org/10.1016/j.atmosres.2025.108489>.

804 Yang, C. Y., Guo, Q.Y., Cao, X.Z., Zhang, W.: Analysis of gravity wave characteristics in the lower
805 stratosphere based on new round-trip radiosonde. Acta Meteorologica Sinica, 2021, 79(1):150-167.
806 doi:<https://doi.org/10.11676/qxxb2021.008>.(in Chinese)

807 Yang, C. Y., Cao, X.Z., Guo, Q.Y., et al. : Feature Extraction and Analysis of Atmospheric Turbulence Based
808 on New Round-Trip Radiosonde [J]. Chinese Journal of Atmospheric Sciences (in Chinese), 2023, 47(6):
809 1967–1982. doi:<https://doi.org/10.3878/j.issn.1006-9895.2202.21103>.(in Chinese)

810 Zhu, H. J., Li, F. Z., Kan, Z. P., He, H., Xiao, D. E., Zhang, L. Q.: Latex balloons buoyancy change analysis and
811 vertical motion trajectory simulation, J. Rubber Ind., 2021, 68(8). doi:<https://doi.org/10.12136/j.issn.1000-890-x.2021.01.0017>. (in Chinese)

813 Zhang, X. P., Guo, Q. Y., Yang, R. K., Ma, X. L., Cao, X. Z.: Assimilation Experiment of Rainstorm in the
814 Middle and Lower Reaches of the Yangtze River Based on "ascent - drift - descent" Sounding Data,
815 Meteorol. Mon., 2021, 47(12), 1512–1524, doi:<https://doi.org/10.7519/j.issn.1000-0526.2021.12.007>. (in
816 Chinese)

817 Zhou, X. S., Guo Q.Y., Xia Y.C., et al.: Inspection of FY-3D satellite temperature data based on horizontal drift
818 round-trip sounding data. J Appl Meteor Sci, 2023, 34(1): 52-64. DOI: 10.11898/1001-7313.20230105.(in
819 Chinese)

820 Zhou, X. S., Hong G., Xia Y.C., Luo H.W., Bao W.Z., Tian H.: Verification of FY-3D Satellite Humidity
821 Profiles Using Descending Phase Data of Round-Trip Drifting Sounding[J].Meteor Mon, 2024,
822 50(11):1373-1385, <http://dx.doi.org/10.7519/j.issn.1000-0526.2024.063002>. (in Chinese)

823 Zhang, C. Z., et al.: Application Experiment of Assimilating Beidou Satellite Navigation Round-Trip Sounding
824 Data Observed in Guangdong Province Using CMA-GD Model, Journal of Tropical Meteorology, 2025,
825 41(1), 16-25, doi:<https://doi.org/10.16032/j.issn.1004-4965.2025.001>.(in Chinese)

- 826 Zhang, X, Wang Q. P, MA, X.L, et al. ; The Influence of New Round-Trip Drifting Sounding Observation on
827 the Quality of Numerical Prediction in the Middle and Lower Reaches of the Yangtze River [J]. Chinese
828 Journal of Atmospheric Sciences, 2025, 49(1): 245–256. doi:[https://doi.org/10.3878/j.issn.1006-](https://doi.org/10.3878/j.issn.1006-9895.2304.22224)
829 9895.2304.22224.(in Chinese)
- 830 Zhang, X. P., Sun, L., Ma, X. L., et al.: Can the Assimilation of the Ascending and Descending Sections' Data
831 from Round-Trip Drifting Soundings Improve the Forecasting of Rainstorms in Eastern China?
832 Atmosphere., 2023, 14, 1127. doi: <https://doi.org/10.3390/atmos14071127>.
- 833 Zhuang, Z. R., Wang, R. C., Wang, J. C., Gong, J. D.: GRAPES_Meso background error characteristics and
834 application, J. Appl. Meteorol. Sci., 2019, 30(3), 316–331, doi:[https://doi.org/10.11898/1001-](https://doi.org/10.11898/1001-7313.20190306)
835 7313.20190306. (in Chinese)
- 836 Zhang, X. F., Li, L. X., Yang, R. K., et al.: Comprehensive Marine Observing Experiment Based on High-
837 Altitude Large Unmanned Aerial Vehicle (South China Sea Experiment 2020 of the “Petrel Project”). Adv.
838 Atmos. Sci. 38, 531–537 (2021). doi:<https://doi.org/10.1007/s00376-020-0314-1>.